

# Effect of the galactic halo modeling on the DAMA/NaI annual modulation result: an extended analysis of the data for WIMPs with a purely spin-independent coupling

P. Belli,<sup>1,\*</sup> R. Cerulli,<sup>1,†</sup> N. Fornengo,<sup>2,‡</sup> and S. Scopel<sup>2,§</sup>

<sup>1</sup>*Dipartimento di Fisica, Università di Roma “Tor Vergata” and INFN,  
Sezione di Roma2, I-00133 Roma, Italy*

<sup>2</sup>*Dipartimento di Fisica Teorica, Università di Torino and INFN,  
Sezione di Torino, Via P. Giuria 1, I-10125 Torino, Italy*

(Dated: February 8, 2020)

## Abstract

The DAMA/NaI Collaboration has observed a  $4\text{-}\sigma$  C.L. model independent effect investigating the annual modulation signature in the counting rate of an NaI(Tl) set-up (total exposure of 57986 kg day) and the implications of this effect have been studied under different model-dependent assumptions. In this paper we extend one of the previous analyses, the case of a WIMP with a purely spin-independent coupling, by discussing in detail the implications on the results of the uncertainties on the dark matter galactic velocity distribution. We study in a systematic way possible departures from the isothermal sphere model, which is the parameterization usually adopted to describe the halo. We specifically consider modifications arising from various matter density profiles, effects due to anisotropies of the velocity dispersion tensor and rotation of the galactic halo. The hypothesis of WIMP annual modulation, already favoured in the previous analysis using an isothermal sphere, is confirmed in all the investigated scenarios, and the effects of the different halo models on the determination of the allowed maximum-likelihood region in the WIMP mass and WIMP-nucleon cross-section are derived and discussed.

---

\*Electronic address: belli@roma2.infn.it

†Electronic address: cerulli@roma2.infn.it

‡Electronic address: fornengo@to.infn.it; URL: <http://www.to.infn.it/~fornengo/>

§Electronic address: scopel@to.infn.it

## I. INTRODUCTION

In the last few years the experiments of direct searches of Weakly Interacting Massive Particles (WIMP) have considerably increased their sensitivity. In particular, the DAMA/NaI Collaboration has collected a very large statistics which allows to look for the distinctive signature in Dark Matter (DM) direct detection represented by the annual modulation of the rate [1, 2, 3], an effect which is due to the rotation of the Earth around the Sun [4]. The analysis of the DAMA/NaI data after 4 years of running [1, 2], corresponding to a total exposure of 57986 kg day, has indeed led to the observation of an annual-modulation effect, which does not appear to be related to any possible source of systematics [3]. This exciting result has been analyzed under different hypotheses on the properties of WIMP dark matter: purely spin independent coupling [1], mixed spin-coherent interaction [5], inelastic dark matter [6]. In the case of purely spin-independent interactions, the annual modulation result has been shown to be compatible with a galactic halo composed, at least partially, by relic neutralinos in different classes of supersymmetric models [7, 8].

In the present analysis we consider the case of a WIMP with coherent interactions dominant over the spin-dependent ones. The analysis of the counting rate of any direct detection experiment may be done in terms of the WIMP mass  $m_W$  and of the quantity  $\xi \sigma_{\text{scalar}}^{(\text{nucleon})}$ , where  $\sigma_{\text{scalar}}^{(\text{nucleon})}$  is the WIMP-nucleon cross section for scalar interaction and  $\xi$ <sup>1</sup> is the fractional amount of local non-baryonic DM density which is ascribed to the WIMP responsible for the effect ( $\xi \leq 1$ ) [1, 7]. Performing a maximum-likelihood analysis of the data, the DAMA/NaI Collaboration has derived a region in the plane  $m_W$ - $\xi \sigma_{\text{scalar}}^{(\text{nucleon})}$  which is compatible at 3- $\sigma$  C.L. to the observed effect of annual modulation. The properties of this region are sensitive to astrophysical inputs [2], some of which deserve a reanalysis and a deeper insight.

One of the main ingredients for the calculation of the expected rates is the distribution function of WIMPs in their six-dimensional phase space:  $F(\vec{r}, \vec{v}) d^3r d^3v$  (where the position vector  $\vec{r} \equiv (x, y, z)$  and the velocity vector  $\vec{v} \equiv (v_x, v_y, v_z)$  are defined in the rest frame of the Galaxy). Direct detection rates  $R_{\text{det}}$  depend on the distribution function (DF) at the Earth position in the Galaxy:

$$f(\vec{v}) \equiv F(\vec{R}_0, \vec{v}), \quad (1)$$

where  $\vec{R}_0 \equiv (R_0, 0, 0)$  is the location of the Earth at a distance  $R_0 \simeq 8.5$  kpc from the galactic center and along the galactic plane. It is therefore clear that an accurate calculation of the expected detection rates requires a knowledge of the phase-space distribution function  $F(\vec{r}, \vec{v}) d^3r d^3v$ .

From the observational side, the most relevant piece of information coming from astro-

---

<sup>1</sup> In Ref. [1] the same symbol indicates a different quantity:  $\xi = \rho_W / 0.3 \text{ GeVcm}^{-3}$ .

physics is related to the rotational velocity of objects bounded to the Galaxy:

$$v_{rot}^2(r) = \frac{GM_{tot}(r)}{r}, \quad (2)$$

where  $G$  is the Newton's constant and  $M_{tot}(r)$  denotes the total mass contained inside the radius  $r \equiv |\vec{r}|$ :

$$M_{tot}(r) = \int_{r' < r} d^3r' \rho_{tot}(\vec{r}'). \quad (3)$$

The rotational velocity therefore depends on the total matter density distribution in space:

$$\rho_{tot}(\vec{r}) = \rho_{DM}(\vec{r}) + \rho_{vis}(\vec{r}), \quad (4)$$

where the DM density distribution function is:

$$\rho_{DM}(\vec{r}) \equiv \int d^3v F(\vec{r}, \vec{v}), \quad (5)$$

and  $\rho_{vis}(\vec{r})$  represents the contribution to the matter density due to components other than the DM, like the disk and the bulge. The local values for the rotational velocity and for the DM matter density are denoted by  $v_0 = v_{rot}(\vec{R}_0)$  and  $\rho_0 \equiv \rho_{DM}(\vec{R}_0)$  and they represent two key parameters in the calculation of WIMP direct detection rates, as it will be discussed in the following.

In order to calculate the DF of Eq. (1) one must invert Eq. (5) taking into account observational data. This problem is affected by degeneracies that cannot be solved without adding some piece of information. This explains why the velocity distribution represents one of the main source of uncertainty in the calculation of direct detection signals.

The usual approach to this problem consists in assuming that the system has some symmetry and that the distribution  $F$  depends on the phase space parameters only through some integrals of motion (energy, angular momentum): this last condition automatically implies stationarity and that the Jeans' equations are verified [9]. The velocity ellipsoid  $\sigma_{ij} \equiv \langle v_i v_j \rangle$  may then be calculated as a function of the derivatives of the potential (which are related to the rotational velocity) by making use of Euler's equation [9]. Physically, this corresponds to impose hydrostatic equilibrium between pressure and gravitational attraction.

The most common and widely used example of such a procedure, and by far the simplest, is the isothermal sphere model. It consists in a spherical infinite system with a flat rotational curve, which automatically implies  $\rho(r) \propto r^{-2}$  and the potential  $\Psi \propto \log(r^2)$ . The DF may be easily worked out, and turns out to be a Maxwellian:  $f(v) \propto \exp(-3v^2/(2v_{rms}^2))$ , where  $v \equiv |\vec{v}|$  and  $v_{rms}$  denotes the root mean squared velocity of the WIMPs. The isothermal sphere describes a self-gravitating gas of collisionless particles in thermal equilibrium, representing the highest entropy rearrangement of WIMPs in their phase space. A strong argument in favour of this last property is the “violent relaxation” model of Lynden-Bell [10], which indicates that the violently changing gravitational field of the newly formed Galaxy may have lead the non-interacting WIMPs to thermal equilibrium. Hydrostatic equilibrium

and the assumption that the velocity ellipsoid is isotropic allows to calculate  $v_{rms}$  through the relation:  $v_{rms}^2 = 3/2 v_{rot}^2(R_0)$ . Due to its simplicity, the isothermal sphere model has become the “standard” assumption in the evaluation of DM expected rates, and has been used extensively in the literature, including the analysis of the DAMA/NaI modulation data [1]. However many of its underlying assumptions (sphericity of the halo, absence of rotation, isotropy of the dispersion tensor, flatness of the rotational curve) are not strongly constrained by astrophysical observations. Moreover the isothermal sphere is strictly unphysical and can only represent the behaviour of the inner part of physical systems, since it has a total infinite mass and needs some cut-off at large radii.

In light of the latest experimental data on WIMP direct searches, the issue of possible departures from the isothermal sphere model has gained interest and prompted several discussions [2, 11]. In the present paper we intend to analyze this issue in a systematic way, by employing a comprehensive set of self-consistent galactic halo models. Each model introduces a different degree of deviation from the simple isothermal sphere. We consider modifications in the velocity distribution function which are originated from a change of the gravitational potential or a change of the DM density profile [12, 13, 14, 15, 16, 17, 18]. We classify the different models depending on the symmetry properties of the galactic halo: spherical potential/density profile with an isotropic velocity dispersion; spherical potential/density profile with a non-isotropic velocity dispersion; axisymmetric models; triaxial models. For the axisymmetric models we also consider the possibility of having a co-rotating or counter-rotating halo.

The plan of the paper is as follows. In section II we introduce the formalism for the calculation of direct detection rates and the annual modulation signal, and summarize the procedure used by the DAMA/NaI Collaboration to determine the annual modulation region in the plane  $m_W - \xi \sigma_{\text{scalar}}^{(\text{nucleon})}$  for a purely spin-dependent WIMP. In Section III we describe the halo models that we intend to discuss and introduce a naming scheme that will be used throughout the paper. Section IV is devoted to the discussion of the constraints on the dark halo of our Galaxy coming from available observational data. In Section V the annual modulation region is calculated in a systematic way for all the models previously introduced, and the results are discussed. Finally, Section VI is devoted to our conclusions.

## II. DIRECT DETECTION RATES AND ANNUAL MODULATION EFFECT

The expected differential event rate of a WIMP direct search experiment is given by the expression:

$$\frac{dR_{det}}{dE_R} = N_T \frac{\rho_0}{m_W} \int d\vec{w} f(\vec{w}) w \frac{d\sigma}{dE_R}(w, E_R) \quad (6)$$

where  $N_T$  is the number of the target nuclei per unit of mass,  $m_W$  is the WIMP mass,  $\vec{w}$  and  $f(\vec{w})$  denote the WIMP velocity and DF in the Earth frame ( $w = |\vec{w}|$ ) and  $d\sigma/dE_R$

is the WIMP–nucleus differential cross section. Notice that the detection rate is directly proportional to the local DM density  $\rho_0$ . The nuclear recoil energy is given by  $E_R = m_{\text{red}}^2 w^2 (1 - \cos \theta^*) / m_N$ , where  $\theta^*$  is the scattering angle in the WIMP–nucleus center-of-mass frame,  $m_N$  is the nuclear mass and  $m_{\text{red}}$  is the WIMP–nucleus reduced mass. Eq.(6) refers to the case of a monoatomic detector, like the Ge detectors. Its generalization to more general situations, like for instance the case of NaI, is straightforward.

The differential cross section can be written as:

$$\frac{d\sigma}{dE_R} = \left( \frac{d\sigma}{dE_R} \right)_{\text{coherent}} + \left( \frac{d\sigma}{dE_R} \right)_{\text{spin-dependent}}. \quad (7)$$

In the rest of this paper we consider only the case of a WIMP with differential cross section dominated by the coherent part. In this case the rate may be expressed in terms of the WIMP – nucleon scalar cross section,  $\sigma_{\text{scalar}}^{(\text{nucleon})}$ , as:

$$\frac{d\sigma}{dE_R} \simeq \left( \frac{d\sigma}{dE_R} \right)_{\text{coherent}} \simeq \frac{F_n^2(E_R)}{E_R^{\text{max}}} \left( \frac{1 + m_W/m_p}{1 + m_W/m_N} \right)^2 A^2 \sigma_{\text{scalar}}^{(\text{nucleon})}, \quad (8)$$

where  $m_p$  and  $m_N$  are the proton and nucleus mass,  $A$  is the nuclear mass number,  $E_R^{\text{max}}$  is the maximal recoil energy and  $F_n(E_R)$  is the nuclear form factor for coherent interactions which may be parametrized with the usual Helm expression [19].

The relation between the velocities  $\vec{v}$  and  $\vec{w}$  is given by:

$$\vec{v} = \vec{v}_{\oplus} + \vec{w}, \quad (9)$$

$$\vec{v}_{\oplus} = \vec{v}_{\odot} + \vec{v}_{\oplus \text{rot}}, \quad (10)$$

where  $\vec{v}_{\oplus}$  and  $\vec{v}_{\odot}$  denote the velocities of the Earth and the Sun in the Galactic rest frame ( $|\vec{v}_{\odot}| \simeq v_0 + 12$  km/sec), and  $\vec{v}_{\oplus \text{rot}}$  is the Earth's orbital velocity around the Sun ( $|\vec{v}_{\oplus \text{rot}}| = 30$  km/sec). Projecting Eq.(10) in the galactic plane, one gets:

$$|\vec{v}_{\oplus}| = |\vec{v}_{\odot}| + |\vec{v}_{\oplus \text{rot}}| \cos \gamma \cos \omega(t - t_0) \quad (11)$$

where  $\gamma$  is the inclination of the plane of rotation with respect to the galactic one,  $\omega = 2\pi/T$  with  $T=1$  year, and  $t_0 \simeq 2^{\text{nd}}$  June corresponds to the day when the Earth's velocity is at its maximum.

The change of reference frame of Eqs. (9,10,11) introduces through the DF  $f(\vec{w})$  a time dependence in the expected rate  $R_{\text{det}}$ . In order to exploit this time-dependence to extract the modulated signal from the measured counting rates, we follow the procedure discussed in detail in Ref. [1]. Indicating with  $N_{ijk}$  the the number of events collected in the  $i$ -th day, the  $k$ -th energy bin and  $j$ -th crystal, the expected value of  $N_{ijk}$  is:

$$\langle N_{ijk} \rangle \equiv \mu_{ijk} = [b_{jk} + S_{0,k} + S_{m,k} \cos \omega(t_i - t_0)] \cdot W_{ijk} \quad (12)$$

where  $b_{jk}$  represents the average background of the  $j$ -th detector in the  $k$ -th energy bin, expressed in number of counts per unit of detector mass, time and interval of collected

energy  $E_{ee}$  (which is related to the recoil energy  $E_R$  by the relation  $E_{ee} = \Theta E_R$  where  $\Theta$  is the quenching factor of the detector) and  $S_{ik} \equiv S_{0,k} + S_{m,k} \cos \omega(t_i - t_0)$  is the corresponding time-dependent signal, approximated by its first order Taylor expansion with respect to  $v_{\oplus rot}$ .  $W_{ijk} = M_j \Delta T_i \Delta E_k \epsilon_{jk}$  are the corresponding exposures, where  $M_j$  is the mass of the  $j$ -th detector,  $\Delta E_k$  is the amplitude of the  $k$ -th energy-bin, while  $\Delta T_i$  represents the  $i$ -th time bin. The  $\epsilon_{jk}$  denote the analysis cut efficiencies. In the following sections the same values of the quenching factors and of the cut efficiencies as in Refs. [1, 2] will be used.

The combined-probability function of all the collected  $N_{ijk}$ , assuming that they have a poissonian distribution with mean values  $\mu_{ijk}$ , is given by:

$$L = \prod_{ijk} e^{-\mu_{ijk}} \frac{\mu_{ijk}^{N_{ijk}}}{N_{ijk}!}. \quad (13)$$

The most probable values of  $m_W$  and  $\sigma_{\text{scalar}}^{(\text{nucleon})}$  maximize  $L$  or, equivalently, minimize the function:

$$\begin{aligned} y(m_W, \sigma) &\equiv -2 \log L - \text{const} \\ &= 2\mu - 2 \sum_{ijk} N_{ijk} \log [b_{jk} + S_{0,k} + S_{m,k} \cos \omega t_i] \end{aligned} \quad (14)$$

where  $\mu \equiv \sum_{ijk} \mu_{ijk}$  and all the parts not depending on  $m_W$  and  $\sigma$  may be absorbed in the constant because are irrelevant for the minimization.

We minimize the function  $y$  in a two-step procedure, first with respect to the time-independent parts  $f_{jk} \equiv b_{jk} + S_{0,k}$  and the functions  $S_{m,k}$ , and then with respect to  $m_W$  and  $\sigma_{\text{scalar}}^{(\text{nucleon})}$  using the  $f_{jk}$  values obtained in the previous step and requiring positive  $b_{jk}$ . Following a standard procedure[20], a region of  $n$  standard deviations around the minimum in the plane  $(\sigma, m_W)$  can be found by imposing the condition  $y(\sigma, m_W) - y_{\min} \leq n^2$ . A lower bound on  $m_W$  at the value  $m_W = 30$  GeV is also applied, to conform to the analysis of Ref.[1, 2].

The data we analyze in the present paper refer to the full set of data released so far by the DAMA/NaI Collaboration [1] (DAMA/NaI 0–4), including also the upper limit on  $\xi \sigma_{\text{scalar}}^{(\text{nucleon})}$  as obtained by the same Collaboration, as discussed in Ref. [1]. We stress that also the determination of upper limits is affected by the choice of the WIMPs DF. This means that also when confronting upper limits one has to specify the galactic halo models which has been considered in the calculation. The formalism introduced in the present paper may in fact be used also to quantify the uncertainty in the determination of upper limits from direct detection experiments.

### III. HALO MODELS

Let us turn now to the discussion of the galactic halo models and of the techniques used to calculate the velocity distribution function  $f(\vec{v})$ . The different models are classified according

to the symmetry properties of their matter density profile (or gravitational potential) and of the velocity distribution function. We define four classes:

- (A) Spherically symmetric matter density with isotropic velocity dispersion;
- (B) Spherically symmetric matter density with non-isotropic velocity dispersion;
- (C) Axisymmetric models;
- (D) Triaxial models.

All the models which we describe in this Section, and that will be used in the rest of the paper, are summarized in Table II, where we also introduce a naming scheme that will be of practical use in the discussion.

#### A. Spherically symmetric matter density with isotropic velocity dispersion

The first class of models is represented by those with a spherically symmetric matter density  $\rho(\vec{r}) = \rho(r)$  and isotropic velocity distribution  $f(\vec{v}) = f(v)$ . These two conditions imply that the phase-space DF depends on the space and velocity variables only through the energy, which is an integral of motion:  $F(\vec{r}, \vec{v}) = F(\epsilon)$ , where  $\epsilon = \Psi(r) - v^2/2$  is the relative energy (per unit mass) of the WIMP and  $\Psi$  is the relative potential, related to the total density  $\rho_{tot}$  through the Poisson's equation [9]:

$$\nabla^2 \Psi = -4\pi G \rho_{tot}. \quad (15)$$

Notice that  $\rho_{tot}$  refers to all the matter components of the Galaxy, like the disk, the bulge or the halo, as written in Eq.(4).

Once the total potential  $\Psi(r)$  is known, the WIMP DF  $F(\epsilon)$  may be worked out by inverting Eq.(5). A change of variables from  $r$  to  $\Psi$  allows to cast Eq.(5) as [9]:

$$4\pi \int_0^\Psi F(\epsilon) \sqrt{2(\Psi - \epsilon)} d\epsilon = \rho_{DM}(\Psi), \quad (16)$$

By performing a Laplace inversion on Eq.(16), one obtains the Eddington formula [9]:

$$F(\epsilon) = \frac{1}{\sqrt{8\pi^2}} \frac{d}{d\epsilon} \int_0^\epsilon \frac{d\rho_{DM}(\Psi)}{d\Psi} \frac{d\Psi}{\sqrt{\epsilon - \Psi}}. \quad (17)$$

In Eqs.(16,17) the normalization of  $\Psi$ , which is defined through Poisson's equation up to an arbitrary constant, is fixed by requiring that  $\Psi(\infty) = 0$ . The velocity distribution function  $f(v)$  which enters the calculation of direct detection rates is then obtained as in Eq.(1).

Eq.(17) shows that the dark matter DF  $F(\vec{r}, \vec{v})$  depends not only on the halo DM density distribution  $\rho_{DM}$ , but also on the density distribution of all the other galactic components.

This has to be the case, since the DM particles move inside the gravitational potential generated by all the matter that makes up the Galaxy. A complete and rigorous determination of the DM DF will therefore require to model not only the galactic halo, but also all the other (disk, bulge) components of the Galaxy (see, for instance Ref. [21]).

However, WIMP direct detection is directly sensitive only to local properties of the Galaxy, and in particular the relevant parameters in the calculation of the detection rate are the local rotational velocity  $v_0$  and the local DM matter density  $\rho_0$ . In fact,  $v_0$  is directly related to the average WIMP kinetic energy, which is relevant in the scattering process with the nuclei of the detector, and the change of reference frame of Eqs. (9,10), which is crucial in determining the amount of annual modulation in the detection rate. Instead,  $\rho_0$  is a sort of normalization factor for the direct detection rate  $R_{det}$ . The dependence of  $R_{det}$  essentially on local parameters implies that a detailed modeling of the inner ( $r \ll R_0$ ) part of the Galaxy, where the disk and bulge components are more relevant and in general dominant over the halo, is not crucial for our analysis. Moreover, the matter density of non-halo components at the local position in the Galaxy ( $r = R_0$ ) are no longer dominant with respect to the halo matter density at the same position (see, for instance Ref. [21]). The bulge, in fact, can be described by using a spheroidal density distribution which gives a sizeable contribution inside the first kpc from the galactic center, and it is truncated at about  $r \simeq 2$  kpc. The disk has an exponential distribution which in most of the models dies away at about 4 kpc from the galactic center. We will therefore assume in the following that in the outer Galaxy the dominant contribution to the matter density is given by the halo:

$$\rho_{vis} \ll \rho_{DM} \quad \text{for } r \gtrsim R_0. \quad (18)$$

The only basic information which is required from the non-halo components is their contribution to the local rotational velocity  $v_0$ :

$$v_0^2 = v_{rot}^2(R_0) = \frac{G}{R_0} [M_{vis} + M_{halo}], \quad (19)$$

where

$$M_{vis \ (halo)} \equiv \int_{r' < R_0} d^3r' \rho_{vis \ (halo)}(r'). \quad (20)$$

A maximal halo occurs when  $M_{vis} \ll M_{halo}$ : in this case almost all the local rotational velocity is supported by the halo and the local DM density  $\rho_0$  gets its maximal value  $\rho_0^{max}$  compatible with the given  $v_0$ . The opposite situation occurs when  $M_{vis}$  assumes its maximal value compatible with observations: in this case, the local rotational velocity gets the maximal contribution from the non-halo components and only a fraction of  $v_0$  is supported by the halo. At the same time  $\rho_0$  gets its minimal value  $\rho_0^{min}$ , for the same  $v_0$ . The constraints on these parameters are discussed in Section IV.

From the point of view of calculating the DM DF (Eq.(17)), the occurrence of a maximal or non-maximal halo modifies the gravitational potential  $\Psi(r)$  and therefore the velocity



distribution function  $f(v)$  is affected. Indicating with  $\Psi_0(r)$  the potential for the maximal halo, the condition of Eq.(18) allows the generalization to the non-maximal case as:

$$\Psi(r) = \frac{\rho_0}{\rho_0^{max}} \Psi_0(r) + \left(1 - \frac{\rho_0}{\rho_0^{max}}\right) \frac{R_0}{r} v_0^2. \quad (21)$$

The condition of Eq. (18) allows to work out the total potential for the case of non-maximal halos without explicitly modeling the visible parts of the Galaxy (bulk, disk): all the dependence of these components are contained in  $M_{vis}$ .

As a comment, we notice that the presence of a non negligible contribution to  $v_0$  from the non-halo components alters also the velocity distribution function of the isothermal sphere. The standard Maxwellian form for the isothermal sphere is in fact correct only for a maximal halo.

Now that we have discussed the procedure to calculate the velocity distribution function once the matter density of the DM is given, we proceed to introduce the different models.

The first type of model is a direct generalization of the isothermal sphere by introducing a core radius  $R_c$ . The density profile is:

$$\rho_{DM}(r) = \frac{v_0^2}{4\pi G} \frac{3R_c^2 + r^2}{(R_c^2 + r^2)^2}, \quad (22)$$

which corresponds to the following potential for a maximal halo:

$$\Psi_0(r) = -\frac{v_0^2}{2} \log(R_c^2 + r^2). \quad (23)$$

From the analytic form of this potential we will refer to this type of models as *logarithmic models*. The usual isothermal sphere corresponds to the limit  $R_c \rightarrow 0$ :

$$\rho_{DM}(r) = \frac{v_0^2}{4\pi G} \frac{1}{r^2}, \quad (24)$$

which corresponds to the following potential for a maximal halo:

$$\Psi_0(r) = -\frac{v_0^2}{2} \log(r^2). \quad (25)$$

For a maximal halo, the velocity distribution function arising from Eqs. (24,25) is the standard Maxwellian one. For a non-maximal halo, a deviation is present also in the  $R_c \rightarrow 0$ , as discussed above. The rotational curve supported by  $\Psi_0$  of Eq. (23) is:

$$v_{rot}^2(r) = v_c^2 \frac{r^2}{(R_c^2 + r^2)}. \quad (26)$$

It is rising for small radii and at large radii becomes flat. In the  $R_C \rightarrow 0$  limit,  $v_{rot} = v_c$  for all radii.

A second type of spherical models is represented by the following matter density [14]:

$$\rho_{DM}(r) = \frac{\beta \Psi_a R_c^\beta}{4\pi G} \frac{3R_c^2 + r^2(1 - \beta)}{(R_c^2 + r^2)^{(\beta+4)/2}}. \quad (27)$$

which corresponds to the following potential for a maximal halo:

$$\Psi_0(r) = \frac{\Psi_a R_c^\beta}{(R_c^2 + r^2)^{\beta/2}} \quad (\beta \neq 0). \quad (28)$$

From the analytic form of this potential we will refer to this type of models as *power-law models*. They represent the spherical limit of the more general class of axisymmetric “power-law” models of Ref. [14] which will be discussed in Section III B. The family of power-law models given by Eq.(28) is not defined for  $\beta = 0$ . However, when  $\beta = 0$  is substituted in Eq. (27), the density of Eq. (22) is recovered. In fact the logarithmic model turns out to have the properties of the “missing”  $\beta = 0$  power law potential. Evaluating Eq.(27) for  $r = R_0$  the parameter  $\Psi_a$  can be expressed in terms of the density  $\rho_0$ . The rotational velocity for the power-law models is given by:

$$v_{rot}^2 = \frac{\beta \Psi_a R_c^\beta r^2}{(R_c^2 + r^2)^{(\beta+2)/2}}, \quad (29)$$

and it is asymptotically falling with  $r$  if  $\beta > 0$  and rising if  $\beta < 0$ .

The last family of spherical models we consider is defined by the following matter density:

$$\rho_{DM} = \rho_0 \left( \frac{R_0}{r} \right)^\gamma \left[ \frac{1 + (R_0/a)^\alpha}{1 + (r/a)^\alpha} \right]^{(\beta-\gamma)/\alpha}. \quad (30)$$

for the choice of values of the parameters  $\alpha$ ,  $\beta$ ,  $\gamma$  and  $a$  summarized in Table I. Except for the Jaffe model, the other three density profiles are obtained from numerical simulations of galaxy evolution.

## B. Spherically symmetric matter density with non-isotropic velocity dispersion

The procedure described in the previous Section can be generalized to the case of a non-isotropic velocity distribution, while keeping a spherically symmetric density profile. In this case, the most general DF is a function of  $\epsilon$  and of the magnitude of the angular momentum vector ( $L = |\vec{L}|$ ):  $F = F(\epsilon, L)$ . Among the different choices which can be performed, a particularly simple case is obtained when  $F$  depends on  $\epsilon$  and  $L$  only through the so called Osipkov–Merrit variable [9, 22]:

$$Q = \epsilon - \frac{L^2}{2r_a^2}, \quad (31)$$

where the parameter  $r_a$  is related to the degree of anisotropy  $\beta_0$  of the velocity dispersion tensor (evaluated at the Earth’s position) in the following way [22]:

$$\beta_0 = 1 - \frac{\bar{v}_\phi^2}{\bar{v}_r^2} = \frac{R_0^2}{R_0^2 + r_a^2}. \quad (32)$$

Here the velocity is expressed in spherical coordinates and  $\bar{v}_\phi = \bar{v}_\theta \neq \bar{v}_r$  (with  $\bar{v}_i^2 \equiv \langle v_i^2 \rangle - \langle v_i \rangle^2$ ,  $i = r, \theta, \phi$ ).

The corresponding DF can be obtained by solving a modified version of Eddington's inversion formula, which is obtained by making the following substitutions in Eq.(17) [9]:

$$\epsilon \rightarrow Q, \quad (33)$$

$$\rho_{DM}(r) \rightarrow \rho_{Q,DM}(r) \equiv \left(1 + \frac{r^2}{r_a^2}\right) \rho_{DM}(r). \quad (34)$$

The models we consider are the same as discussed in Section III A: the logarithmic model of Eq. (22), the power-law models of Eqs. (27) and the models defined by Eq.(30). The velocity distribution functions, which are obtained by solving the Eddington equation with the Osipkov-Merrit term, are therefore anisotropic with a degree of anisotropy controlled by the parameter  $\beta_0$  related to  $r_a$  as in Eq.(32).

### C. Axisymmetric models

In the case of axial symmetry the DF depends in general (at least) on two integrals of motion, the relative binding energy  $\epsilon$  and the component  $L_z$  of the angular momentum along the axis of symmetry. The DF may be written quite generally as the sum of an even ( $F_+$ ) and an odd ( $F_-$ ) contribution with respect to  $L_z$ :

$$F(\epsilon, L_z) = F_+(\epsilon, L_z) + F_-(\epsilon, L_z), \quad (35)$$

where:

$$F_\pm = \frac{1}{2} [F(\epsilon, L_z) \pm F(\epsilon, -L_z)]. \quad (36)$$

When Eq.(16) is extended to the axisymmetric case, the density  $\rho_{DM}$  turns out to depend only on the even part  $F_+$  [9], so that, by inverting it, the DF may be determined up to an arbitrary odd part  $F_-$ . The problem of the determination of  $F_+$  for an axisymmetric matter density is both analytically and numerically hard to perform and actually it requires a double Laplace inversion on Eq.(16). However, for particular families of axisymmetric potentials this problem has been solved analytically by Evans [13, 14]. These families are the axisymmetric generalization of the first two classes already introduced in Section III A: the first family has a logarithmic potential, the second one has a power-law potential. We stress that these analytic solution for  $F_+$  are obtained under the assumption that the halo potential is dominant over the other components. Therefore these solutions correspond to a maximal halo. Even though they do not represent the most general situation, their simplicity makes them of practical use and convenient for studying the axisymmetric case.

The first family of axisymmetric potential we consider is the *logarithmic potential* [13]:

$$\Psi_0(R, z) = -\frac{v_0^2}{2} \log(R_c^2 + R^2 + \frac{z^2}{q^2}), \quad (37)$$

where  $R^2 = x^2 + y^2$  is the radial coordinate along the galactic plane,  $R_c$  is the core radius and  $q$  the flatness parameter. The corresponding DM density is:

$$\rho_{DM}(R, z) = \frac{v_0^2}{4\pi G q^2} \frac{(2q^2 + 1)R_c^2 + R^2 + (2 - q^{-2})z^2}{(R_c^2 + R^2 + z^2 q^{-2})^2}. \quad (38)$$

Eqs.(37) and (38) are the axisymmetric generalization of Eqs. (23) and (22). The corresponding rotational curve is obtained from Eq.(26) by substituting the radial coordinate  $r$  with the radial coordinate in the galactic plane  $R$ .

By expressing  $z$  as a function of  $\Psi$  through Eq.(37), the density of Eq.(38) may be decomposed as [14]:

$$\rho = \rho_0(\Psi) + R^2 \rho_1(\Psi), \quad (39)$$

which allows to determine  $F_+$  in the form:

$$F_+(\epsilon, L_z) = F_+^0(\epsilon) + L_z^2 F_+^1(\epsilon), \quad (40)$$

leading to a particularly simple analytic solution for the DF [13]. We give it for completeness in Appendix A. The relation of Eq.(39) is no longer valid for a non-maximal halo, since in that case, the change of variable from  $z$  to  $\Psi$  is not determined by the potential of Eq.(37) but by an axisymmetric analogous of Eq.(21). Therefore the analytic expression given by Eq.(40) can be used only for maximal halos, *i.e.*  $\rho_0 = \rho_0^{max}$ .

The second family of distribution functions is a generalization of the axisymmetric logarithmic potential to the case of an asymptotically non-flat rotational curve, while preserving the property of Eq. (39). This is obtained for the axisymmetric *power-law potential* [14]:

$$\Psi_0(R, z) = \frac{\Psi_a R_c^\beta}{(R_c^2 + R^2 + z^2 q^{-2})^{\beta/2}} \quad (\beta \neq 0). \quad (41)$$

The corresponding matter density is:

$$\rho_{DM}(R, z) = \frac{\beta \Psi_a R_c^\beta}{4\pi G q^2} \frac{(2q^2 + 1)R_c^2 + (1 - \beta q^2)R^2 + [2 - q^{-2}(1 + \beta)]z^2}{(R_c^2 + R^2 + z^2 q^{-2})^{(\beta+4)/2}}. \quad (42)$$

Evaluating Eq.(42) for  $R = R_0$ ,  $z = 0$  the parameter  $\Psi_a$  can be expressed in terms of the density  $\rho_0$ . Eqs.(41) and (42) are the axisymmetric generalization of Eqs. (28) and (27) and they possess the same properties already discussed in Section III A. As for the case of the logarithmic potential, the rotational curve is obtained from Eq.(29) by substituting the radial coordinate  $r$  in Eq.(29) with the radial coordinate in the galactic plane  $R$ , and it is asymptotically falling with  $R$  if  $\beta > 0$  and rising if  $\beta < 0$ .

In analogy with the logarithmic case, also for the power-law model an analytic solution for the DF can be worked out [14] with the form of Eq. (40). This applies again only for a maximal halo. The analytic formulas for  $F_+$  can be found for completeness in Appendix A.

### 1. Co-rotation and counter-rotation of the halo

As mentioned before, the DF for an axisymmetric model is known up to an arbitrary odd component  $F_-$ . The DF we summarized above for the Evans's models all refer to the pure even component: they all have  $F_-(\epsilon, L_z) = 0$  and possess no bulk rotation. The case  $F_-(\epsilon, L_z) \neq 0$  corresponds to the case of a rotating halo, where the number of particles moving clockwise around the axis of symmetry is different from that in the opposite sense.

A family of DF's with bulk rotation can be studied by constructing an explicit example for  $F_-$ . This can be done, starting from a generic  $F_+$ , by considering the linear combination [23, 24, 25]:

$$F_-(\epsilon, L_z) = F_{right}(\epsilon, L_z) - F_{left}(\epsilon, L_z), \quad (43)$$

where

$$F_{right}(\epsilon, L_z) = \begin{cases} F_+(\epsilon, L_z), & v_\phi > 0, \\ 0, & v_\phi < 0, \end{cases} \quad (44)$$

and

$$F_{left}(\epsilon, L_z) = \begin{cases} 0, & v_\phi > 0, \\ F_+(\epsilon, L_z), & v_\phi < 0, \end{cases} \quad (45)$$

The distributions  $F_{right}$  and  $F_{left}$  describe the configurations with maximal  $|\bar{v}_\phi|$  with the same density profile as  $F_+$  [23]. A DF with an intermediate value of  $\bar{v}_\phi$  can be obtained as a linear combination of  $F_+$  and  $F_-$ , or, equivalently, of  $F_{left}$  and  $F_{right}$ :

$$F(\epsilon, L_z) = \eta F_{right}(\epsilon, L_z) + (1 - \eta) F_{left}(\epsilon, L_z). \quad (46)$$

The parameter  $\eta$  ranges from 1 (maximal co-rotation) to 0 (maximal counter-rotation) and is related to the dimensionless spin parameter  $\lambda$  of the Galaxy by:  $\lambda = 0.36|\eta - 0.5|$  [24]. In order to be consistent with the available extensive numerical work on galaxy formation,  $\lambda$  should not exceed the value 0.05 [26], implying  $0.36 \lesssim \eta \lesssim 0.64$ . For all the Evans model discussed in this Section, we will also study the co- and counter- rotating situations, adopting the two values  $\eta = 0.36$  and  $\eta = 0.64$ .

### D. Triaxial models

The last class of models we wish to discuss is represented by the *triaxial potential* discussed in Ref. [15]:

$$\Psi_0(x, y, z) = -\frac{1}{2}v_0^2 \log \left( x^2 + \frac{y^2}{p^2} + \frac{z^2}{q^2} \right), \quad (47)$$

which, for a maximal halo, corresponds to the DM density:

$$\rho_{DM}(x, y, z) = \frac{v_0^2}{4\pi G} \frac{Ax^2 + By^2/p^2 + Cz^2/q^2}{(x^2 + y^2/p^2 + z^2/q^2)^2} \quad (48)$$

where  $A = p^{-2} + q^{-2} - 1$ ,  $B = 1 + q^{-2} - p^{-2}$  and  $C = 1 + p^{-2} - q^{-2}$ . In Ref. [15] the velocity DF  $f(\vec{v})$  of the system is approximated by a triaxial Gaussian with semiaxes equal to the velocity dispersions as obtained by the solutions of the Jeans equations:

$$\bar{v}_r^2 = \frac{v_0^2}{(2 + \delta)(p^{-2} + q^{-2} - 1)} \quad (49)$$

$$\bar{v}_\theta^2 = \frac{v_0^2(2q^{-2} - 1)}{2(p^{-2} + q^{-2} - 1)} \quad (50)$$

$$\bar{v}_\phi^2 = \frac{v_0^2(2p^{-2} - 1)}{2(p^{-2} + q^{-2} - 1)} \quad (51)$$

when the Earth's position is on the major axis of the equipotential ellipsoid, and:

$$\bar{v}_r^2 = \frac{v_0^2 p^{-4}}{(2 + \delta)(1 + q^{-2} - p^{-2})} \quad (52)$$

$$\bar{v}_\theta^2 = \frac{v_0^2(2q^{-2} - p^{-2})}{2(1 + q^{-2} - p^{-2})} \quad (53)$$

$$\bar{v}_\phi^2 = \frac{v_0^2(2 - p^{-2})}{2(1 + q^{-2} - p^{-2})} \quad (54)$$

when the Earth's position is on the intermediate axis. In Eqs.(49,52) the quantity  $\delta$  is a free parameter that in the spherical limit ( $p = q = 1$ ) quantifies the degree of anisotropy of the velocity dispersion tensor:

$$\frac{\bar{v}_\phi^2}{\bar{v}_r^2} = \frac{2 + \delta}{2}. \quad (55)$$

#### IV. CONSTRAINING THE MODELS

Once a given model is chosen for the velocity distribution function of the dark matter particles, the parameters of the model have to be fixed using observational data. Unfortunately, due to its “darkness”, all our knowledge of the halo is of indirect nature [21, 27] and it includes requirements on the circular rotational speed (constraints on its flatness and its value at the solar circle and in the outer regions of the Galaxy) as well as observational constraints on the local surface density of the disk and on the dispersion velocity of the bulge. In general, one should construct a composite model of the Galaxy where the DM is coupled to other components like the disk and the bulge, and the parameters describing the various components are varied independently requiring that the observational constraints are satisfied.

We have already noticed that WIMP direct detection rates are particularly sensitive to the value of the rotational velocity  $v_0$  and the local DM density  $\rho_0$  (both evaluated at the solar circle). The procedure we follow in order to determine the allowed ranges for  $v_0$  and  $\rho_0$  in each galactic model is explained in the following. First of all, the experimental informations we use are: the allowed range for the local rotational velocity, the amount of flatness of

the rotational curve of our Galaxy and the maximal amount of non-halo components in the Galaxy. The first information directly fixes the allowed interval for  $v_0$ , irrespective of the galactic halo model. The other constraints are used in order to determine the allowed ranges for  $\rho_0$ , for each halo model.

The allowed interval for  $v_0$  is:

$$v_0 = (220 \pm 50) \text{ km sec}^{-1} \quad (90\% \text{ C.L.}), \quad (56)$$

which conservatively relies on purely dynamical observations [28]. Proper motion measurements of nearby stars [29] lead to similar estimates for the central value of  $v_0$ , with a significantly smaller uncertainty. However they are based on the assumption of circular orbit of the observed objects. For definiteness, we will use in the following three representative values for  $v_0$ , which correspond to its central value and to the boundaries of its allowed 90% C.L. range of Eq.(56):  $v_0 = 170, 220, 270 \text{ km sec}^{-1}$ .

For the three representative values of  $v_0$  we then determine the corresponding allowed ranges for  $\rho_0$ . For each halo model and for each value of  $v_0$ , we calculate, as a function of  $\rho_0$ , two quantities: (i) the total amount of mass  $M_{vis}$  in components other than the halo (*e.g.* : disk, bulge) which is necessary in order to match the given value of local rotational velocity  $v_0$ ; (ii) the value of the rotational curve at a distance of 100 kpc from the center of the Galaxy:  $v_{rot}^{100} \equiv v_{rot} (R = 100 \text{ kpc})$ . These two quantities are somewhat constrained from observations, even though their constraints are often obtained by using some degree of galactic modeling. We conservatively quote the following ranges [21, 27]:

$$1 \cdot 10^{10} M_{\odot} \lesssim M_{vis} \lesssim 6 \cdot 10^{10} M_{\odot} \quad (57)$$

$$0.8 \cdot v_0 \lesssim v_{rot}^{100} \lesssim 1.2 \cdot v_0. \quad (58)$$

where  $M_{\odot}$  denotes the solar mass. The first constraint limits the amount of non-halo components, while the second is a constraints of “essentially flatness” rotational curve: only galactic halo models which provide a rotational curve which does not deviate from a flat one more than 20% at 100 kpc are accepted. The constraint of Eq.(58) is compatible with the estimates of the galactic mass at large radii as obtained by the dynamics of satellites of the Galaxy [21].

The behaviour of  $M_{vis}$  and  $v_{rot}^{100}$  as a function of  $\rho_0$  is shown in Fig. 1 (which refers to  $v_0 = 220 \text{ km s}^{-1}$ ), Fig. 2 ( $v_0 = 170 \text{ km s}^{-1}$ ) and Fig. 3 ( $v_0 = 270 \text{ km s}^{-1}$ ). Each line refers to a different halo model. The upper panels show that  $M_{vis}$  is a decreasing function of  $\rho_0$ , since increasing the amount of dark matter in the Galaxy implies that less matter in other galactic components is required to support the rotational curve. On the other hand, the value of the rotational velocity in the outer Galaxy is totally supported by the dark halo, and it is larger for more massive haloes.

When the constraints expressed in Eqs. (57) and (58) are simultaneously applied, an allowed interval for  $\rho_0$  may be derived for each halo model.

The procedure outlined above may be used as a simple recipe for identifying the intervals for the local density parameter. However, some caution must be taken in the application of the bounds on  $M_{vis}$  in Eq.(57). As already discussed in the previous Section, for the models of class A and class B we solve the Eddington equation in order to determine the velocity distribution function of dark matter particles. In this case we can take into account also the situation in which the local rotational velocity is only partially supported by the halo, and therefore we can apply the limits to  $M_{vis}$  given by Eq.(57). Instead, the analytic models of class C and class D may be applied only to the extreme case of a fully maximal-halo, since the analytic formulae for  $f(\vec{v})$  are derived under the assumption that only the halo matter density is present. For these models (class C and class D) the only case we can deal with is that of a fully maximal halo, which corresponds to  $M_{vis} = 0$ . This represents a conservative upper limit for  $\rho_0$ . From Fig. 1–3 we can see that the difference in the upper bounds to  $\rho_0$  obtained from the  $M_{vis} = 0$  limit are only a few percent larger than what is obtained by imposing the lower limit of Eq.(57):  $M_{vis} = 1 \cdot 10^{10} M_\odot$ . For consistency and simplicity, we will use  $M_{vis} \simeq 0$  as a lower limit also for models of class A and B.

The allowed intervals for  $\rho_0$  that we obtain by imposing the bounds on  $M_{vis}$  and  $v_{rot}^{100}$  are listed in Table III. As discussed above, both values  $\rho_0^{min}$  and  $\rho_0^{max}$  will be used in the next Sections to perform the modulation analysis of the DAMA/NaI experimental data, while only  $\rho_0^{max}$  will be used for the analysis of the data for models of class C and D. We stress that the reason for this stands in the fact that for the analytic models of classes C and D, we know  $f(\vec{v})$  only for a maximal-halo.

## V. RESULTS AND DISCUSSION

In this Section we make use of the halo models described in Section III, with the choice of parameters shown in Table II, to analyze the annual-modulation signal present in the DAMA/NaI data [1] in terms of relic WIMPs with purely coherent interactions. The procedure is the one outlined in Section II. The results are presented as  $3\sigma$  annual-modulation regions shown in the plane  $\xi\sigma_{\text{scalar}}^{(\text{nucleon})}$  versus  $m_W$ . All figures are divided in three panels which correspond to the cases:  $v_0 = 170, 220, 270 \text{ km sec}^{-1}$ .

A general feature of all the models is that by raising the parameter  $v_0$  the modulation region moves from the upper-right to the lower-left of the  $m_W$ – $\xi\sigma_{\text{scalar}}^{(\text{nucleon})}$  plane. This is easily understood since, for a given DM density profile, higher values of  $v_0$  imply higher values of  $\rho_0$  (through Eq. (2)) and of the velocity ellipsoid  $\sigma_{ij} \equiv \langle v_i v_j \rangle$  (through the Jeans equations); the experimental value of the signal and the measured WIMP–nucleus recoil energy are fixed by the data, therefore the modulation region moves downward because:

$$\frac{dR_{det}}{dE_R} \propto \rho_0 \times \sigma_{\text{scalar}}^{(\text{nucleon})} \quad (59)$$



(see Eq. (6)) and moves to lower masses because:

$$E_R \propto m_W \times \langle v^2 \rangle. \quad (60)$$

On the other hand, when one compares the different density profiles that we have discussed in the previous Sections, it is worth noticing that, for a given value of  $v_0$ , a stronger singularity in the galactic center lowers the value of  $\rho_0^{max}$  (in order to keep constant the mass integral) with the consequence that the lower part of the modulation region rises. So the smallest values of  $\xi\sigma_{\text{scalar}}^{(\text{nucleon})}$  are reached by the models with a less singular density profile.

Figures 4–18 show the result of the analysis for the models with a spherically symmetric density profile (models A0–7, B1–7). Models A0–7 have an isotropic velocity dispersion, while in models B1–7 a degree of anisotropy in the velocity dispersion is introduced through the Osipkov–Merrit term of Eq.(31). The amount of anisotropy is controlled by the  $\beta_0$  parameter of Eq. (32) and it has been fixed at the value:  $\beta_0 = 0.4$ . This value corresponds to a radial anisotropy. In order to account for the uncertainty in the DM local density  $\rho_0$ , for each case two regions are given, the lower (higher) corresponding to  $\rho_0 = \rho_0^{min}$  ( $\rho_0^{max}$ ), where  $\rho_0^{min}$  and  $\rho_0^{max}$  have been obtained as discussed in Section IV and are reported in Table III. The numerical values of the parameters summarized in the third column of Table II have been chosen in order to ensure the compatibility of the curves of Figs. 1, 2, 3 with the constraints of Eqs.(57,58), discussed in Section IV. The Jaffe models A4, B4, which goes into the isothermal sphere when  $R_c \rightarrow \infty$ , have been calculated for the smallest allowed value of the core radius  $R_c$  in order to examine the case of maximal departure from the usual scenario. As a consequence of this, for this model  $\rho_0^{min} \simeq \rho_0^{max}$  and in Figs. 8,15 the upper and lower modulation regions are superimposed.

The effect of radial anisotropy in the velocity dispersion tensor ( $\bar{v}_r > \bar{v}_\theta = \bar{v}_\phi$ ), which occurs for the models of class B, may be seen by comparing Figs. 5–11 with the corresponding Figs. 12–18. As a general feature, a reduction of the modulation effect is expected, since the WIMPs phase space is depopulated along the direction of the Sun’s velocity. This is confirmed by the fact that in most cases the modulation regions move upwards and widens, although the size of the effect can be small. The effect of radial anisotropy on the WIMP mass is more involved. In particular, the modulation regions for models B1, B3, B5, B6 extend to heavier WIMP masses compared to the corresponding isotropic cases, while for models B2, B4, B7 the region moves to smaller WIMP masses.

As already pointed out, for the models belonging to classes C and D only the regions for  $\rho_0 = \rho_0^{max}$  are shown. As far as the axisymmetric models of class C are concerned, they are shown in Fig. 19, 22, 25, 28. In each model the flatness parameter  $q$  has been chosen in order to have the maximal flatness compatible with observations and with the positivity of the DF. The main effect induced by flatness is through the increase in the local density  $\rho_0$ , as can be seen in Table III. As a consequence, the modulation regions for these models reach values of  $\xi\sigma_{\text{scalar}}^{(\text{nucleon})}$  significantly below the levels of the spherical cases. In Figs. 20, 23, 26, 29 the same models are shown with a co-rotation effect of the halo implemented through Eq.(46)

with  $\eta = 0.64$ , while in Figs. 21, 24, 27, 30 for the same models a counter-rotation effect with  $\eta = 0.36$  has been introduced. The main consequence of halo co-rotation is a decrease of the relative velocity between WIMPs and the Earth. The energy of WIMPs is therefore smaller and in order to produce the same recoil energy in the detector the WIMPs have to be heavier. This can be verified in the figures, where the modulation region of co-rotating models may reach very high WIMP masses, even higher than 200 GeV. By the same token, in counter-rotating models the modulation region is shifted toward lower masses.

The peculiar shape of the modulation region of Fig. 20 deserves some comments. The two disconnected closed contours, which arise at different  $m_W$  values, are indicative of the superposition in the WIMP phase space of two components with well separated r.m.s. velocities. This is exemplified in Fig. 35 for the models B1 ( $q = 1$ ) and C1 ( $q = 1/\sqrt{2}$ ), where the contour plots of the corresponding DF's are plotted in the  $v-v_\phi$  plane (in the galactic rest frame) and in the  $w-w_\phi$  plane (in the Earth's rest frame). It is evident from the figure that, in flattened models, small  $|L_z|$  orbits are depopulated compared to the spherical case, leading to two well separated populations with  $v_\phi > 0$  and  $v_\phi < 0$ . These two components have the same temperature in the galactic rest frame, but develop different r.m.s. velocities when boosted in the Earth's rest frame. As shown in Fig. 35, the relative weight of the two populations can be tilted towards fast or slow WIMPs in the two cases of a co-rotating or counter-rotating halo, respectively. This explains why the co-rotating model of Fig. 20 develops a second minimum at high WIMP masses, and this is not observed in the corresponding non-rotating or counter-rotating cases. We have numerically verified that the peculiar disconnected region at high WIMP masses reduces in size when the flatness parameter is increased (since in this way the velocity distribution function becomes more similar to the non-flattened one), while it shifts towards lower masses when the core radius  $R_c$  is decreased.

We conclude the discussion of our results with the triaxial models shown in Figs. 31, 32, 33, 34 where, to be definite, the same choice of parameters of Ref.[15] is adopted. For these models a general solution for the DF is not available. Only the velocity ellipsoid of Eq. (49–52) is known, and it is used to fix the second moments of a non-isotropic Maxwellian. This explains why the shape of the modulation regions is quite similar to the standard case. In models D1 and D2 the Earth is assumed to be located on the major axis of the density ellipsoid, while in models D3 and D4 it is placed on the intermediate axis. Since in the two cases the Sun's position  $R_0$  is the same,  $\rho_0$  is higher for models D1, D2 than for models D3, D4 (see Table III). As a consequence, the modulation regions of Fig. 31, 32 reach smaller values of  $\xi\sigma_{\text{scalar}}^{(\text{nucleon})}$  compared to those of Figs. 33, 34. Models D1 and D3 (D2 and D4) have  $\delta = -1.78$  ( $\delta = 16$ ), which implies a radial (tangential) anisotropy of the velocity ellipsoid (see Eq. (55)). Solving the Jeans equation for the potential of Eq.(47) in the spherical limit  $q = p = 1$  (which corresponds to a non-cored isothermal sphere) leads to the relation [9]:

$$v_\phi^2 + v_\theta^2 = \frac{3}{2}v_0^2. \quad (61)$$

Note that this property is a consequence of the flatness of the rotational curve, and would not be true, for instance, including a core radius in the potential. Eq.(61) implies that, in this model, the tangential components of the velocity ellipsoid are fixed by  $v_0$ . As a consequence of this, radial anisotropy ( $v_r > v_\theta = v_\phi$ ) corresponds to faster WIMPs and tangential anisotropy to slower WIMPs. This shifts the modulation regions towards smaller values of  $m_W$  in Figs. 31, 33 and higher values of  $m_W$  in Figs. 32, 34. This effect is sizeable in the case of tangential anisotropy, where the modulation region may extend up to  $m_W \simeq 270$  GeV.

The results of this section are summarized in Fig. 36, where all the modulation regions previously discussed have been plotted jointly. A convolution of all the regions may be indicative of the uncertainties in the determination of the WIMP modulation signal due to the modeling of the WIMP DF. As a final result, we show such a convolution in Fig. 37, where a single curve in the plane  $m_W$ – $\xi\sigma_{\text{scalar}}^{(\text{nucleon})}$  is plotted by collecting the information contained in the analyses of all the non-rotating models considered in this paper. The region is compared with the original annual modulation region obtained in Ref. [1] for an isothermal sphere model of the galactic halo with rotational velocity  $v_0 = 220$  km s<sup>−1</sup> and local dark matter density  $\rho_0 = 0.3$  GeV cm<sup>−3</sup>. From Fig.37 we see that the DAMA/NaI annual modulation result is compatible with WIMPs masses up to  $m_W \simeq 270$  GeV and WIMP–nucleon cross sections in the interval:  $10^{-10}$  nbarn  $\lesssim \xi\sigma_{\text{scalar}}^{(\text{nucleon})} \lesssim 6 \times 10^{-8}$  nbarn when the uncertainties in the WIMP velocity DF is taken into account. Co-rotating models with maximal corotation can extend the mass range even further, up to  $m_W \simeq 500$ – $900$  GeV, for cross section of the order  $\text{few} \times 10^{-9}$  nbarn  $\lesssim \xi\sigma_{\text{scalar}}^{(\text{nucleon})} \lesssim 2 \times 10^{-8}$  nbarn, as it can be seen, for instance, in Fig. 36.

## VI. CONCLUSIONS

In the present paper we have extended a previous analyses of the DAMA modulation experiment for the case of a WIMP with a purely spin-independent coupling, by discussing in detail the implications on the results of the uncertainties on the dark matter galactic velocity distribution. We have studied a large number of viable models which deviate from the standard isothermal sphere in the matter density profile, in the presence of anisotropies of the velocity dispersion tensor and in effects of rotation of the galactic halo. The different models have been classified according to the symmetry properties of their matter density profile (or gravitational potential) and of the velocity distribution function. We have specifically considered: (a) spherically symmetric matter density with isotropic velocity dispersion; (b) spherically symmetric matter density with non-isotropic velocity dispersion; (c) axisymmetric models; (d) triaxial models.

The different models have then been used to re-analyze the DAMA/NaI 0–4 data collected by the DAMA/NaI Collaboration [1]; in particular a total exposure of 57986 kg day, which

corresponds to 4 annual cycles, has led to the observation of an annual modulation effect. The hypothesis of WIMP annual modulation, already favoured in the previous studies [1, 2] by using an isothermal sphere, is confirmed in all the investigated scenarios, and the effects of the different halo models on the determination of the allowed maximum-likelihood region in the WIMP mass and WIMP-nucleon cross-section have been derived. We can summarize that the DAMA/NaI annual modulation result is compatible with WIMPs masses up to  $m_W \simeq 270$  GeV and WIMP-nucleon cross sections in the interval:  $10^{-10}$  nbarn  $\lesssim \xi \sigma_{\text{scalar}}^{(\text{nucleon})} \lesssim 6 \times 10^{-8}$  nbarn, when the uncertainties in the WIMP velocity DF is taken into account. When also co-rotation of the galactic halo is considered, the mass range extends further to  $m_W \simeq 500\text{--}900$  GeV, for cross section of the order  $\text{few} \times 10^{-9}$  nbarn  $\lesssim \xi \sigma_{\text{scalar}}^{(\text{nucleon})} \lesssim 2 \times 10^{-8}$  nbarn. These intervals quantify the extent of the annual modulation region for WIMPs with purely spin-independent couplings, as due to uncertainties in the phase space distribution function of galactic WIMPs.

## Acknowledgements

We thank Prof. R. Bernabei and Prof. A. Bottino for useful discussions and suggestions. We are indebted with the DAMA/NaI Collaboration for allowing us to use its data for this investigation.

## APPENDIX A: AXISYMMETRIC MODELS

In this appendix we give, for completeness, the analytic formulas of the DF's for the axisymmetric potentials of Eqs. (37,41) adapted from Refs. [13, 14]. All expressions are written in the reference frame of the Galaxy.

### 1. Logarithmic potential

The DF for the logarithmic potential of Eq. (37) can be written as:

$$F(\epsilon, L_z^2) = (A + B) \exp\left(\frac{-2v^2}{v_0^2}\right) + C \exp\left(\frac{-v^2}{v_0^2}\right), \quad (\text{A1})$$

where:

$$A = F_0 4\pi \left(\frac{2}{\pi}\right)^{5/2} \left(\frac{v_\phi}{v_0}\right)^2 \frac{R_0^4}{(R_0^2 + R_c^2)^2} \frac{1 - q^2}{q^2}, \quad (\text{A2})$$

$$B = F_0 4\pi \left(\frac{2}{\pi^5}\right)^{1/2} \frac{R_0^2 R_c^2}{(R_0^2 + R_c^2)^2} \frac{1}{q^2}, \quad (\text{A3})$$

$$C = F_0 \frac{R_0^2}{R_0^2 + R_c^2} \frac{2q^2 - 1}{q^2}, \quad (\text{A4})$$

and  $F_0 = 0.47 \text{ GeV cm}^{-3}/v_0^3$ .

## 2. Power-law potential

The DF for the power-law potential of Eq. (41) for  $\beta > 0$  can be written as:

$$F(\epsilon, L_z^2) = A\tilde{\epsilon}^{4/\beta-3/2} + B\tilde{\epsilon}^{4/\beta-1/2} + C\tilde{\epsilon}^{2/\beta-1/2}, \quad (\text{A5})$$

where:

$$\tilde{\epsilon} \equiv \frac{\epsilon}{\Psi_a} = \frac{\Psi - \frac{1}{2}v^2}{\Psi_a} = \zeta^2 - \frac{1}{2} \left( \frac{v}{v_1} \right)^2, \quad (\text{A6})$$

with  $\zeta = R_c/\sqrt{R_c^2 + R_0^2}$ , while the velocity  $v_1 = \sqrt{|\Psi_a|}$  is fixed through Eq. (42), and with suitable normalizations, can be cast in the form:

$$v_1 = 220 \text{ km sec}^{-1} \left( \frac{\rho_0}{0.47 \text{ GeV cm}^{-3}} \right)^{\frac{1}{2}} \frac{R_0}{8.5 \text{ kpc}} \frac{q(R_c^2 + R_0^2)^{(\beta+4)/4}}{\sqrt{|\beta|R_0R_c^{\beta/2}}\sqrt{R_c^2(1+2q^2) + R_0^2(1-\beta q^2)}}, \quad (\text{A7})$$

The quantities  $A$ ,  $B$  and  $C$  may be written as:

$$A = F_1 \left( \frac{v_\phi}{220 \text{ km sec}^{-1}} \right)^2 \left( \frac{R_0}{R_c} \right)^4 \frac{\Gamma(2+4/\beta)}{2^{3/2}\pi^{3/2}\Gamma(4/\beta-1/2)} \beta(\beta+2) \left( \frac{1}{q^2} - 1 \right), \quad (\text{A8})$$

$$B = F_1 \left( \frac{v_1}{220 \text{ km sec}^{-1}} \right)^2 \left( \frac{R_0}{R_c} \right)^2 \frac{\Gamma(2+4/\beta)}{2^{3/2}\pi^{3/2}\Gamma(1/2+4/\beta)} \beta(\beta+2) \frac{1}{q^2}, \quad (\text{A9})$$

$$C = F_1 \left( \frac{v_1}{220 \text{ km sec}^{-1}} \right)^2 \left( \frac{R_0}{R_c} \right)^2 \frac{\Gamma(2+2/\beta)}{2^{3/2}\pi^{3/2}\Gamma(1/2+2/\beta)} \beta \left[ 2 - \frac{1+\beta}{q^2} \right], \quad (\text{A10})$$

with  $F_1 = 0.47 \text{ GeV cm}^{-3}/v_1^3$ .

For  $\beta < 0$  Eq. (A5) still applies, with the following modifications (now  $\Psi_a < 0$ ):

$$\tilde{\epsilon} \equiv \frac{-\epsilon}{\Psi_a} = -\frac{\Psi + \frac{1}{2}v^2}{\Psi_a} = \zeta^2 - \frac{1}{2} \left( \frac{v}{v_1} \right)^2, \quad (\text{A11})$$

where:

$$A = F_1 \left( \frac{v_\phi}{220 \text{ km sec}^{-1}} \right)^2 \left( \frac{R_0}{R_c} \right)^4 \frac{\Gamma(3/2-4/\beta)}{2^{3/2}\pi^{3/2}\Gamma(-1-4/\beta)} \beta(\beta+2) \left( 1 - \frac{1}{q^2} \right), \quad (\text{A12})$$

$$B = F_1 \left( \frac{v_1}{220 \text{ km sec}^{-1}} \right)^2 \left( \frac{R_0}{R_c} \right)^2 \frac{\Gamma(1/2-4/\beta)}{2^{3/2}\pi^{3/2}\Gamma(-1-4/\beta)} \beta(\beta+2) \frac{1}{q^2}, \quad (\text{A13})$$

$$C = F_1 \left( \frac{v_1}{220 \text{ km sec}^{-1}} \right)^2 \left( \frac{R_0}{R_c} \right)^2 \frac{\Gamma(1/2-2/\beta)}{2^{3/2}\pi^{3/2}\Gamma(-1-2/\beta)} \beta \left[ \frac{1+\beta}{q^2} - 2 \right], \quad (\text{A14})$$

with again  $F_1 = 0.47 \text{ GeV cm}^{-3}/v_1^3$ .

- 
- [1] R. Bernabei *et al.* (DAMA/NaI Collaboration), Phys. Lett. **B424**, 195 (1998); Phys. Lett. **B450**, 448 (1999); Phys. Lett. **B480**, 23 (2000).
  - [2] P. Belli, R. Bernabei, A. Bottino, F. Donato, N. Fornengo, D. Prospero and S. Scopel, Phys. Rev. D **61**, 023512 (2000) [arXiv:hep-ph/9903501].
  - [3] R. Bernabei *et al.*, Eur. Phys. J. **C18**, 283 (2000).
  - [4] A.K. Drukier, K. Freese, and D.N. Spergel, Phys. Rev. D **33**, 3495 (1986); K. Freese, J. A. Frieman and A. Gould, Phys. Rev. D **37**, 3388 (1988).
  - [5] R. Bernabei *et al.* (DAMA/NaI Collaboration), Phys. Lett. **B509**, 197 (2001).
  - [6] R. Bernabei *et al.* (DAMA/NaI Collaboration), Eur. Phys. J. **C 23**, 61 (2001).
  - [7] A. Bottino, F. Donato, N. Fornengo and S. Scopel, Phys. Lett. **B423**, 109 (1998) [arXiv:hep-ph/9709292]; Phys. Rev. D **59**, 095003 (1999) [arXiv:hep-ph/9808456]; Phys. Rev. D **59**, 095004 (1999) [arXiv:hep-ph/9808459]; Phys. Rev. D **62**, 056006 (2000) [arXiv:hep-ph/0001309]; Phys. Rev. D **63**, 125003 (2001) [arXiv:hep-ph/0010203].
  - [8] R. Arnowitt and P. Nath, Phys. Rev. D **60**, 044002 (1999) ; E. Accomando, R. Arnowitt, B. Dutta and Y. Santoso, Nucl. Phys. **B585**, 124 (2000) [arXiv:hep-ph/0001019]; R. Arnowitt, B. Dutta and Y. Santoso, arXiv:hep-ph/0008336; J.L. Feng, K. Matchev and F. Wilczek, Phys. Lett. **B482**, 388 (2000) [arXiv:hep-ph/0004043]; E. Gabrielli, S. Khalil, C. Muñoz and E. Torrente-Lujan, Phys. Rev. D **63**, 025008 (2001) [arXiv:hep-ph/0006266]; D.G. Cerdeño, S. Khalil and C. Muñoz, arXiv:hep-ph/0105180; D.G. Cerdeño, E. Gabrielli, S. Khalil, C. Muñoz and E. Torrente-Lujan, Nucl. Phys. **B603**, 231 (2001) [arXiv:hep-ph/0102270]; M.E. Gómez and J.D. Vergados, Phys. Lett. **B512**, 252 (2001) [arXiv:hep-ph/0012020].
  - [9] J. Binney and S. Tremaine, *Galactic Dynamics*, Princeton Univ. Press , Princeton, 1987.
  - [10] D. Lynden-Bell, Mon. Not. R. Astron. Soc. **136**, 101 (1967).
  - [11] J.D. Vergados, Phys. Rev. **83** (1998) 3597, Phys. Rev. D **62** (2000) 023519; P. Ullio and M. Kamionkowski, JHEP **03**, 049 (2001); A. M. Green, Phys. Rev. D **63**, 043005 (2001); J.D. Vergados and D. Owen, arXiv:astro-ph/0203293.
  - [12] W. Jaffe, Mon. Not. R. Astron. Soc. **202**, 995 (1983)
  - [13] N. W. Evans, Mon. Not. R. Astron. Soc. **260**, 191 (1993).
  - [14] N. W. Evans, Mon. Not. R. Astron. Soc. **267**, 333 (1994).
  - [15] N.W. Evans, C.M. Carollo and P.T. de Zeeuw, Mon. Not. R. Astron. Soc. **318**, 1131 (2000).
  - [16] J. F. Navarro, C. S. Frenk and S. D. M. White, Astrophys. J. **462**, 563 (1996).
  - [17] B. Moore *et al.*, Mon. Not. R. Astron. Soc. **310**, 1147 (1990).
  - [18] A. V. Kravtsov *et al.*, Astrophys. J. **502**, 48 (1998).
  - [19] R. H. Helm, Phys. Rev. **104**, 1466 (1956).
  - [20] D. E. Groom *et al.* (Particle Data Group Collaboration), Eur. Phys. J. **C15**, 1 (2000).
  - [21] W. Dehnen and J. Binney, Mon. Not. R. Astron. Soc. **294**, 429 (1998).

- [22] L. P. Osipkov, *Pris'ma Astron.* **55**, 77 (1979); D. Merrit, *Astrophys. J.* **90**, 1027 (1985).
- [23] D. Lynden–Bell, *Mon. Not. R. Astron. Soc.* **120**, 204 (1960).
- [24] M. Kamionkowski and A. Kinkhabwala, *Phys. Rev. D* **57** (1998) 3256.
- [25] F. Donato, N. Fornengo and Scopel, *Astrop. Phys.* **9**, 333 (1999).
- [26] S. Warren, P. J. Quinn, J. K. Salmon and W. H. Zurek, *Astrophys. J.* **399**, 405 (1992); S. Cole and C. Lacey, *Mon. Not. R. Astron. Soc.* **281**, 7126 (1996).
- [27] E. I. Gates, G. Gyuk, M. S. Turner, *Phys. Rev. D* **53**, 4138 (1996).
- [28] C. S. Kochanek, *Astrophys. J.* **457**, 228 (1996).
- [29] M. Feast and P. Whitelock, *Mon. Not. R. Astron. Soc.* **291**, 683 (1997).

TABLE I: Values of the parameters for the spherically symmetric density profile of Eq.(30).

	$\alpha$	$\beta$	$\gamma$	$a$ (kpc)
NFW [16]	1	3	1	20
Moore et al. [17]	1.5	3	1.5	28
Kravtsov et al. [18]	2	3	0.4	10
Jaffe [12]	1	4	2	160



TABLE II: Summary of the galactic halo models discussed in Section III. The label introduced in the first column is used throughout the text to indicate each model in a unique way. For all the models the numerical values of the parameters which have been used in the calculations are given in the third column. The last column contains references to the models in the text. Models of class C have been analyzed also including co-rotation and counter-rotation of the halo through Eq. (46).

<b>Class A: Spherical <math>\rho_{\text{DM}}</math>, isotropic velocity dispersion</b>			
A0	Isothermal sphere		Eq.(24)
A1	Evans' logarithmic [13]	$R_c = 5 \text{ kpc}$	Eq.(22)
A2	Evans' power-law [14]	$R_c = 16 \text{ kpc}, \beta = 0.7$	Eq.(27)
A3	Evans' power-law [14]	$R_c = 2 \text{ kpc}, \beta = -0.1$	Eq.(27)
A4	Jaffe [12]	Table I	Eq.(30)
A5	NFW [16]	Table I	Eq.(30)
A6	Moore et al. [17]	Table I	Eq.(30)
A7	Kravtsov et al. [18]	Table I	Eq.(30)
<b>Class B: Spherical <math>\rho_{\text{DM}}</math>, non-isotropic velocity dispersion (Osipkov-Merriit, <math>\beta_0 = 0.4</math>)</b>			
B1	Evans' logarithmic	$R_c = 5 \text{ kpc}$	Eqs.(22,32)
B2	Evans' power-law	$R_c = 16 \text{ kpc}, \beta = 0.7$	Eqs.(27,32)
B3	Evans' power-law	$R_c = 2 \text{ kpc}, \beta = -0.1$	Eqs.(27,32)
B4	Jaffe	Table I	Eqs.(30,32)
B5	NFW	Table I	Eqs.(30,32)
B6	Moore et al.	Table I	Eqs.(30,32)
B7	Kravtsov et al.	Table I	Eqs.(30,32)
<b>Class C: Axisymmetric <math>\rho_{\text{DM}}</math></b>			
C1	Evans' logarithmic	$R_c = 0, q = 1/\sqrt{2}$	Eqs.(37,38)
C2	Evans' logarithmic	$R_c = 5 \text{ kpc}, q = 1/\sqrt{2}$	Eqs.(37,38)
C3	Evans' power-law	$R_c = 16 \text{ kpc}, q = 0.95, \beta = 0.9$	Eqs.(41,42)
C4	Evans' power-law	$R_c = 2 \text{ kpc}, q = 1/\sqrt{2}, \beta = -0.1$	Eqs.(41,42)
<b>Class D: Triaxial <math>\rho_{\text{DM}}</math> [15] (<math>q = 0.8, p = 0.9</math>)</b>			
D1	Earth on major axis, radial anisotropy	$\delta = -1.78$	Eqs.(47,48)
D2	Earth on major axis, tangential anis.	$\delta = 16$	Eqs.(47,48)
D3	Earth on intermediate axis, radial anis.	$\delta = -1.78$	Eqs.(47,48)
D4	Earth on intermediate axis, tangential anis.	$\delta = 16$	Eqs.(47,48)

TABLE III: Allowed intervals of  $\rho_0$  obtained from the constraints on  $M_{vis}$  and  $v_{rot}^{100}$  for the halo models summarized in Table II. The values of  $\rho_0^{max}$  and  $\rho_0^{min}$  are used in the modulation analysis of the experimental data of Figs. 4–18 for the models of class A and B, while only  $\rho_0^{max}$  is used for models of class C and D in Figs. 19–34. The value of  $\rho_0^{max}$  for the axisymmetric models of class C are not affected by the inclusion of a co-rotation or counter-rotation effect through Eq.(46).

	$v_0 = 170 \text{ km sec}^{-1}$		$v_0 = 220 \text{ km sec}^{-1}$		$v_0 = 270 \text{ km sec}^{-1}$	
Model	$\rho_0^{min}$	$\rho_0^{max}$	$\rho_0^{min}$	$\rho_0^{max}$	$\rho_0^{min}$	$\rho_0^{max}$
A0	0.18	0.28	0.30	0.47	0.45	0.71
A1 , B1	0.20	0.42	0.34	0.71	0.62	1.07
A2 , B2	0.24	0.53	0.41	0.89	0.97	1.33
A3 , B3	0.17	0.35	0.29	0.59	0.52	0.88
A4 , B4	0.26	0.27	0.44	0.45	0.66	0.67
A5 , B5	0.20	0.44	0.33	0.74	0.66	1.11
A6 , B6	0.22	0.39	0.37	0.65	0.57	0.98
A7 , B7	0.32	0.54	0.54	0.91	0.82	1.37
C1	0.36	0.56	0.60	0.94	0.91	1.42
C2	0.34	0.67	0.56	1.11	0.98	1.68
C3	0.30	0.66	0.50	1.10	0.97	1.66
C4	0.32	0.65	0.54	1.09	0.96	1.64
D1 , D2	0.32	0.50	0.54	0.84	0.81	1.27
D3 , D4	0.19	0.30	0.32	0.51	0.49	0.76

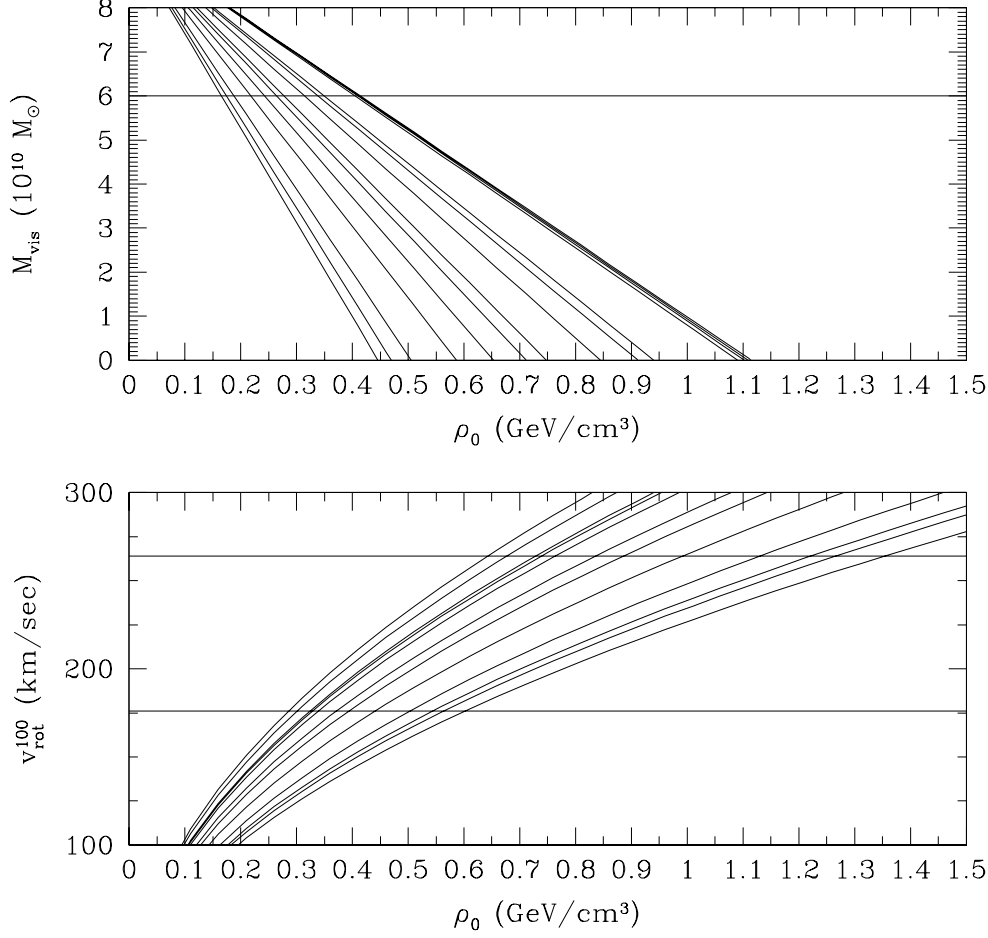


FIG. 1: The quantities  $M_{vis}$  (upper panel) and  $v_{rot}^{100} \equiv v_{rot}(R = 100 \text{ kpc})$  (lower panel) calculated as a function of  $\rho_0$  for the halo models summarized in Table II and for  $v_0 = 220 \text{ km sec}^{-1}$ . The different curves correspond, from left to right, to the following halo models: A4, A0, D3, A3, A6, A1, A5, D1, A7, C1, C4, C3, A2, C2 (upper panel); A3, A0, D3, A5, A1, A6, A2, A4, C3, A7, C2, C1 (lower panel: here C4 and D1 are not plotted because indistinguishable from A7). The horizontal lines indicate the constraints discussed in Section IV. The B1-7 models have the same density distribution of the corresponding A1-7 models. D2 and D4 have the same distribution as D1 and D3, respectively.

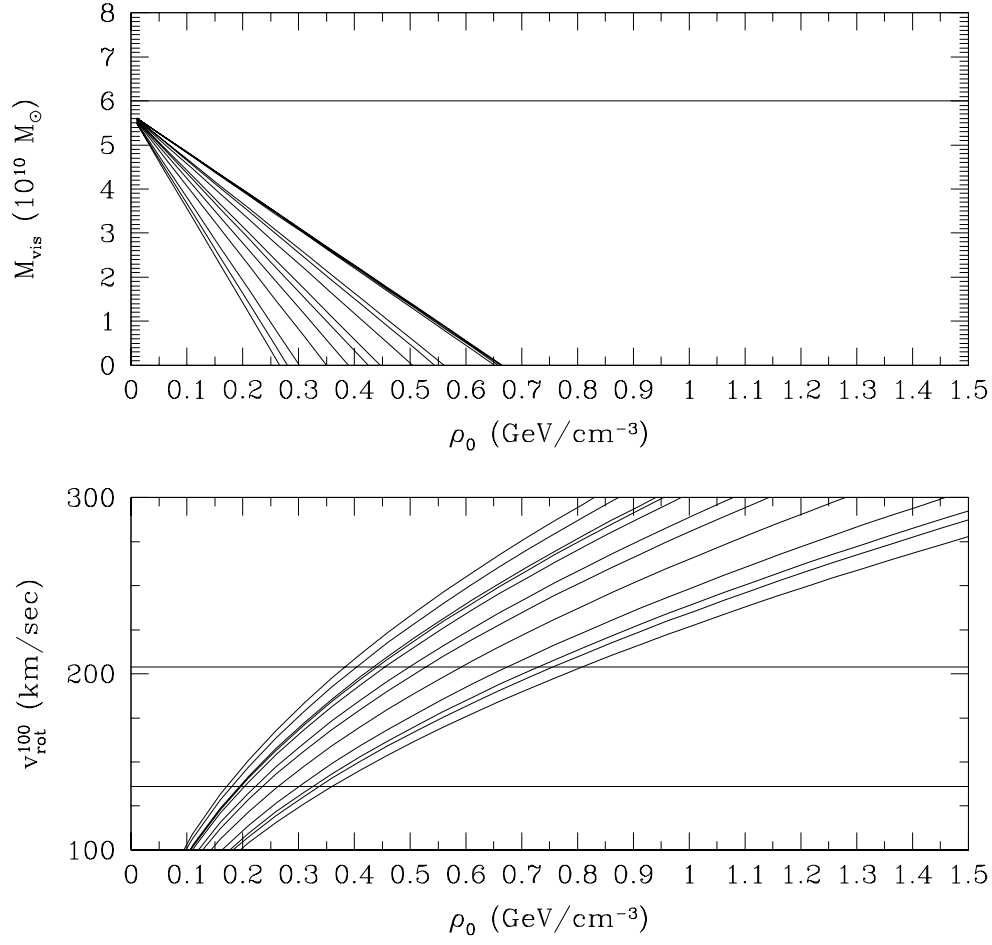


FIG. 2: The same as in Figure 1 for  $v_0 = 170 \text{ km sec}^{-1}$  (the ordering of all the different curves is maintained).

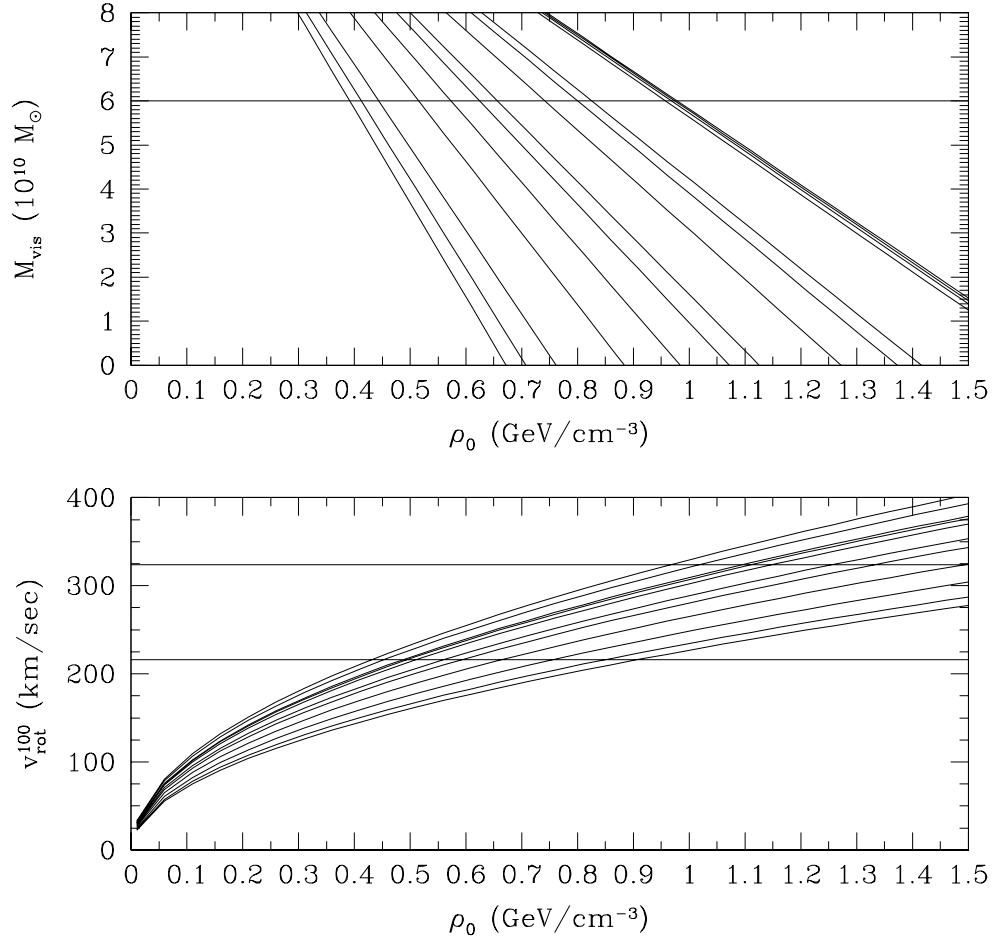


FIG. 3: The same as in Figure 1 with  $v_0 = 270 \text{ km sec}^{-1}$  (the ordering of all the different curves is maintained).

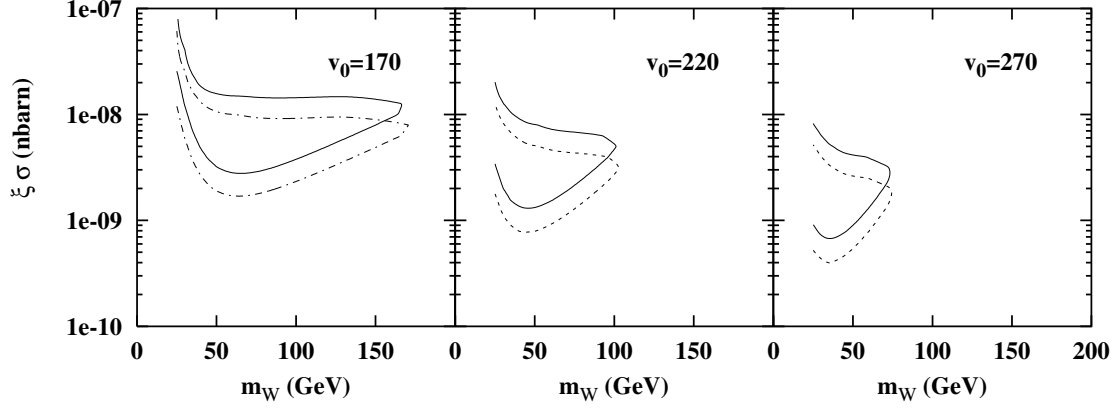


FIG. 4: Plot of the  $3\sigma$  annual-modulation region in the plane  $\xi\sigma_{\text{scalar}}^{(\text{nucleon})}$  versus  $m_W$  using for the velocity distribution of WIMPs the isothermal sphere model (Model A0, see Table II). The three panels of the figure correspond to  $v_0=170, 220, 270$  km sec $^{-1}$  from left to right. Upper (lower) regions correspond to  $\rho_0=\rho_0^{\min}$  ( $\rho_0^{\max}$ ) where  $\rho_0^{\min}$  and  $\rho_0^{\max}$  are given in Table III.

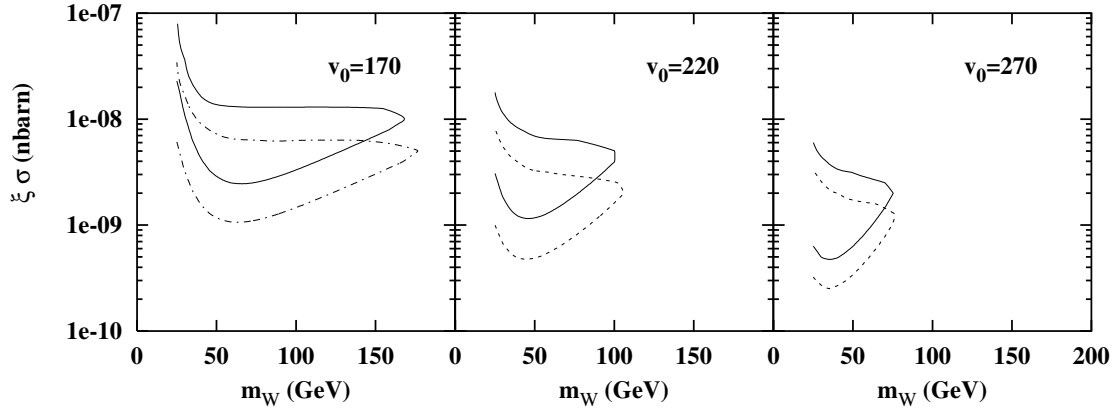


FIG. 5: The same as in Fig. 4 for the velocity distribution of model A1 (see table II).

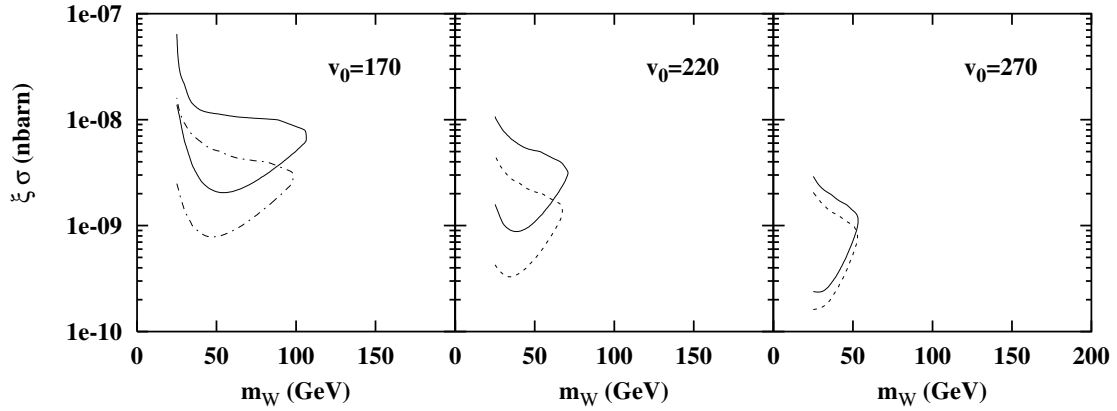


FIG. 6: The same as in Fig. 4 for the velocity distribution of model A2.

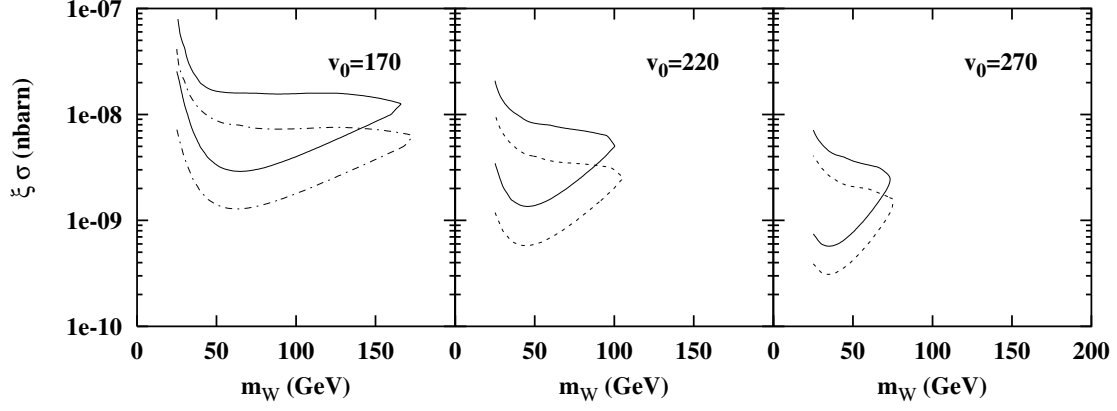


FIG. 7: The same as in Fig. 4 for the velocity distribution of model A3.

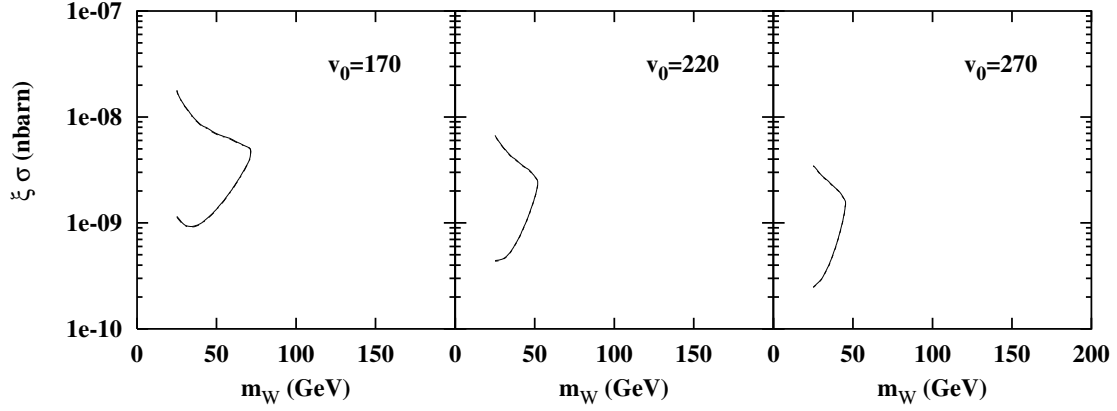


FIG. 8: The same as in Fig. 4 for the velocity distribution of model A4. In this case  $\rho_0^{max} \simeq \rho_0^{min}$ , so upper and lower curves are not distinguishable.

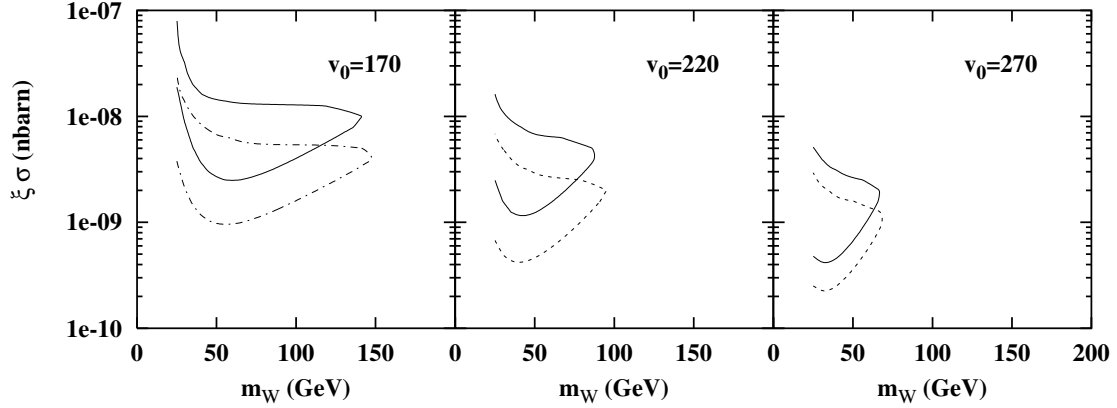


FIG. 9: The same as in Fig. 4 for the velocity distribution of model A5.

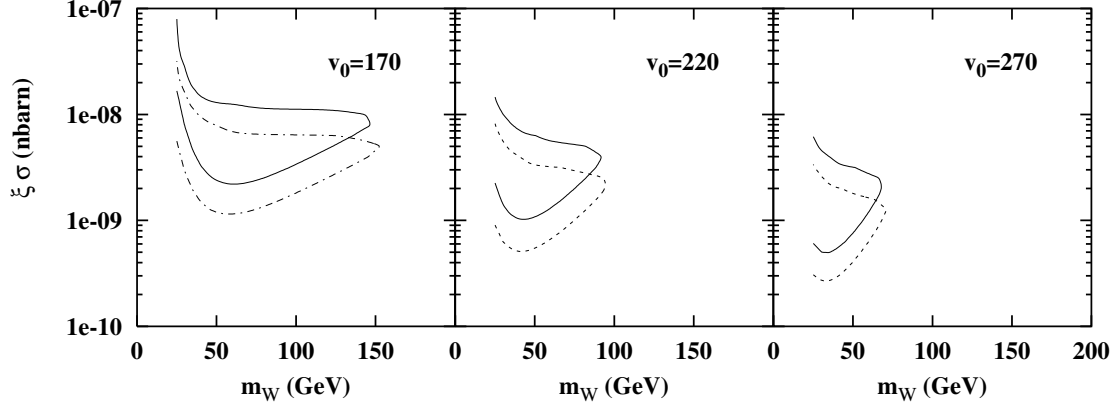


FIG. 10: The same as in Fig. 4 for the velocity distribution of model A6.

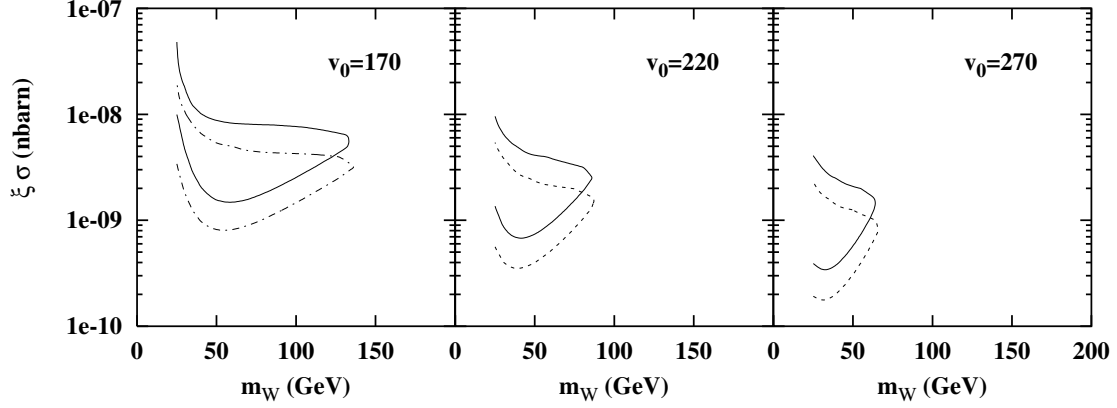


FIG. 11: The same as in Fig. 4 for the velocity distribution of model A7.

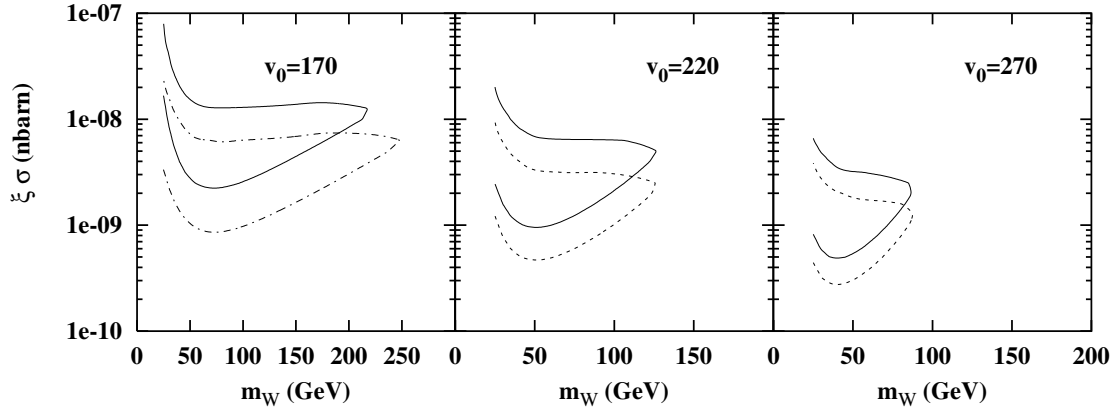


FIG. 12: The same as in Fig. 5, with anisotropy of the velocity dispersion through the Osipkov–Merrit term and anisotropy parameter  $\beta_0 = 0.4$  (model B1). The horizontal axis has been extended in the first panel.



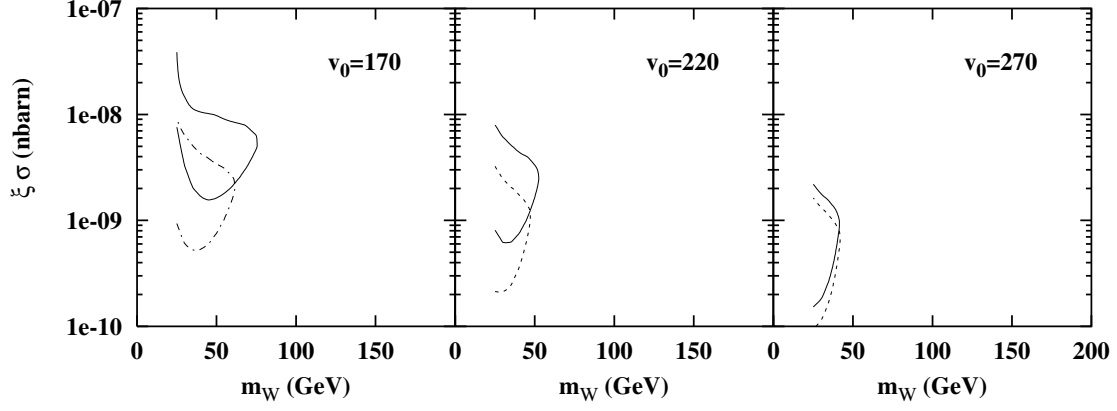


FIG. 13: The same as in Fig. 6, with anisotropy of the velocity dispersion through the Osipkov–Merrit term and anisotropy parameter  $\beta_0 = 0.4$  (model B2).

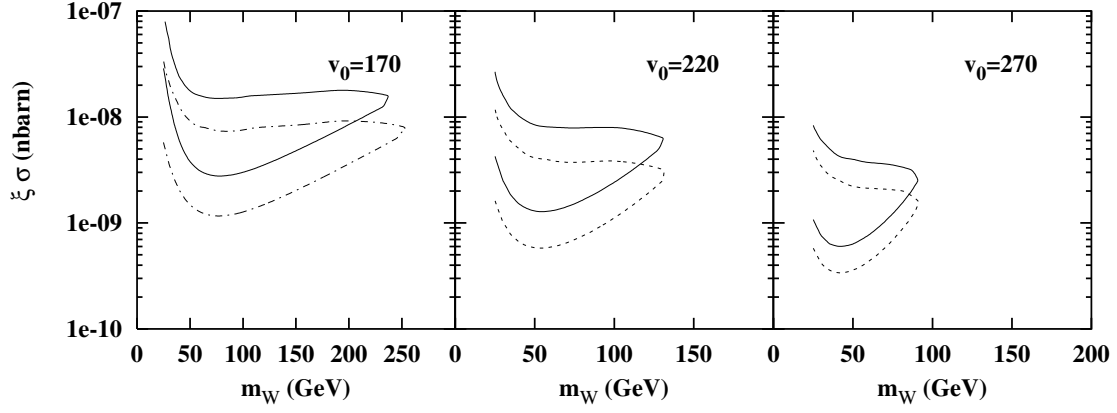


FIG. 14: The same as in Fig. 7, with anisotropy of the velocity dispersion through the Osipkov–Merrit term and anisotropy parameter  $\beta_0 = 0.4$  (model B3). The horizontal axis has been extended in the first panel.

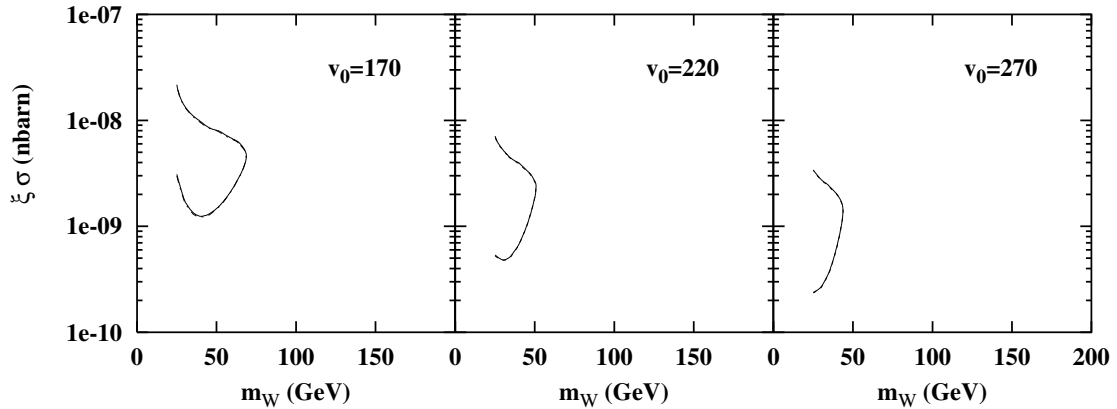


FIG. 15: The same as in Fig. 8, with anisotropy of the velocity dispersion through the Osipkov–Merrit term and anisotropy parameter  $\beta_0 = 0.4$  (model B4). In this case  $\rho_0^{max} \simeq \rho_0^{min}$ , so upper and lower curves are not distinguishable.

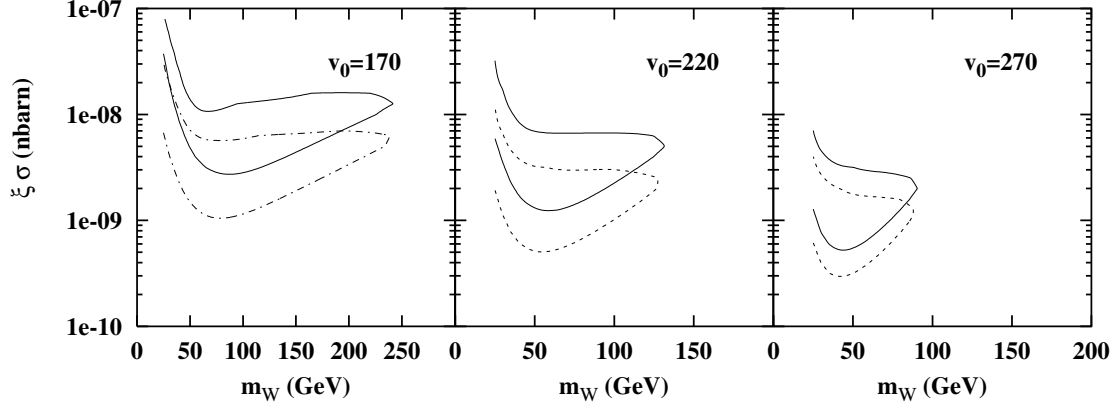


FIG. 16: The same as in Fig. 9, with anisotropy of the velocity dispersion through the Osipkov-Meritt term and anisotropy parameter  $\beta_0 = 0.4$  (model B5). The horizontal axis has been extended in the first panel.

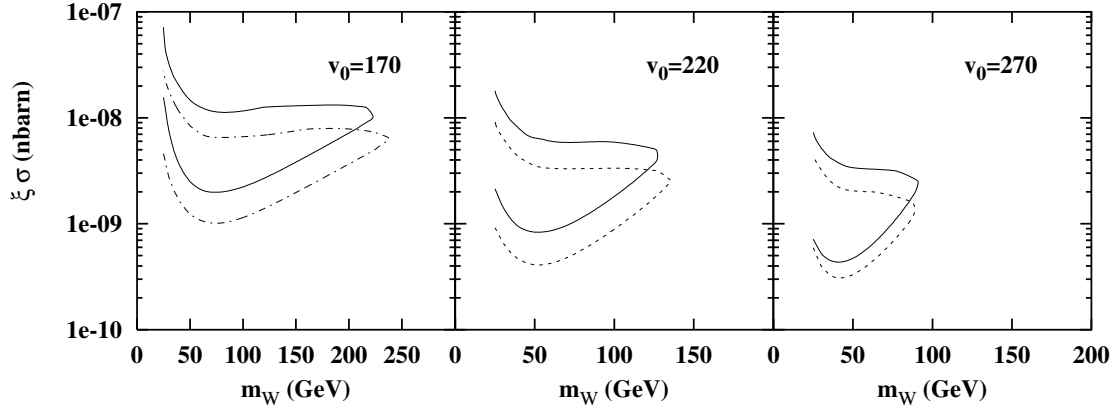


FIG. 17: The same as in Fig. 10, with anisotropy of the velocity dispersion through the Osipkov-Meritt term and anisotropy parameter  $\beta_0 = 0.4$  (model B6). The horizontal axis has been extended in the first panel.

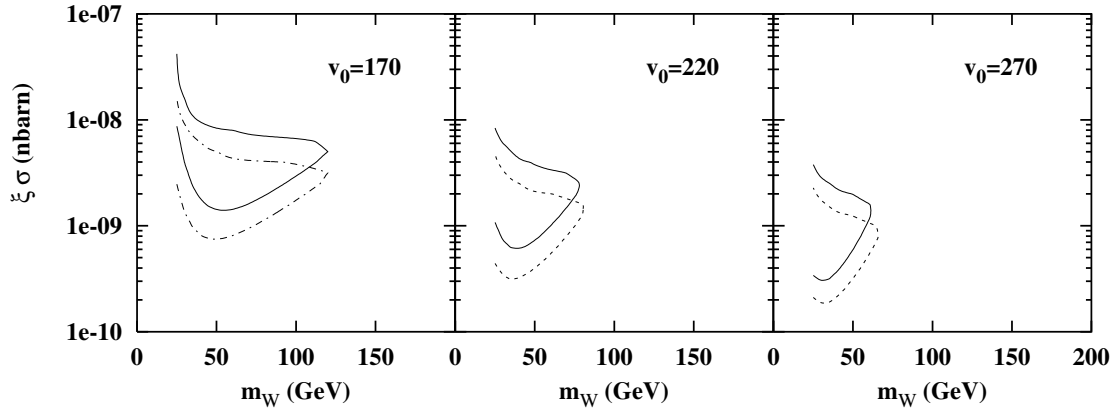


FIG. 18: The same as in Fig. 11, with anisotropy of the velocity dispersion through the Osipkov-Meritt term and anisotropy parameter  $\beta_0 = 0.4$  (model B7).

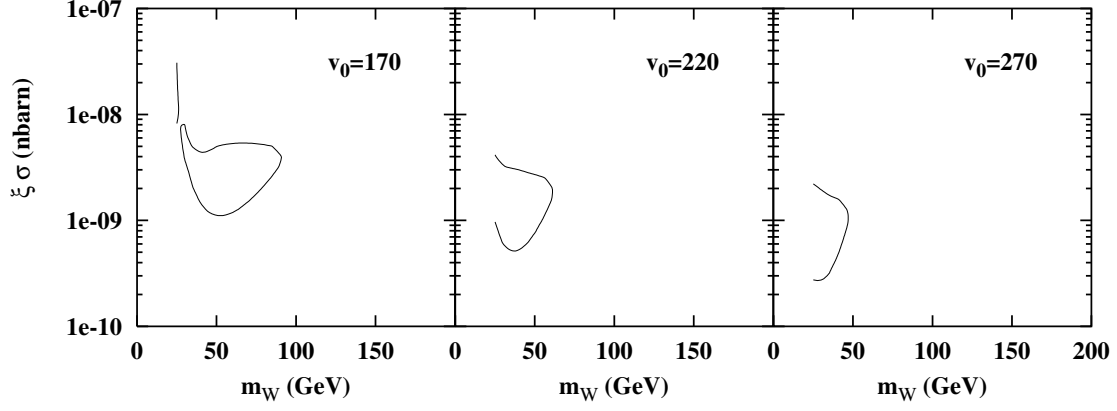


FIG. 19: The same as in Fig. 4 for the velocity distribution of model C1. Only the case  $\rho_0 = \rho_0^{max}$  is shown.

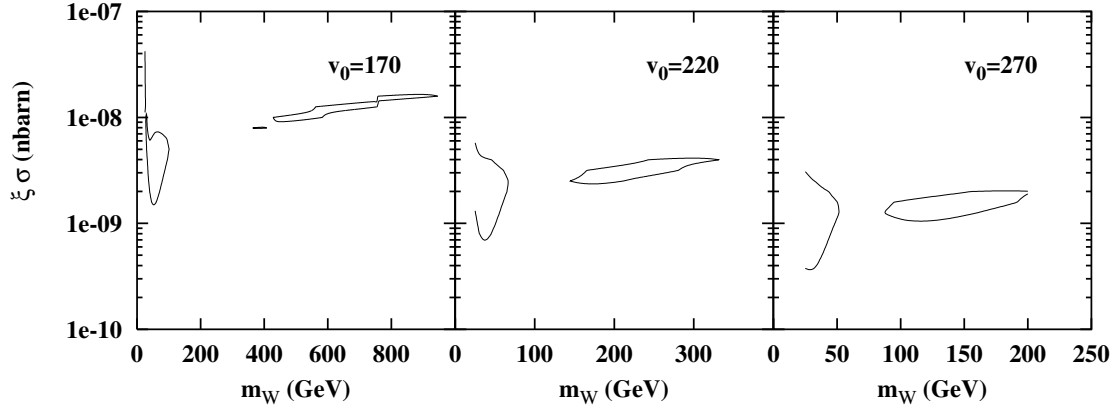


FIG. 20: The same as in Fig. 19 including a co-rotation effect of the halo with  $\eta = 0.64$ . The horizontal axis has been extended in all panels.

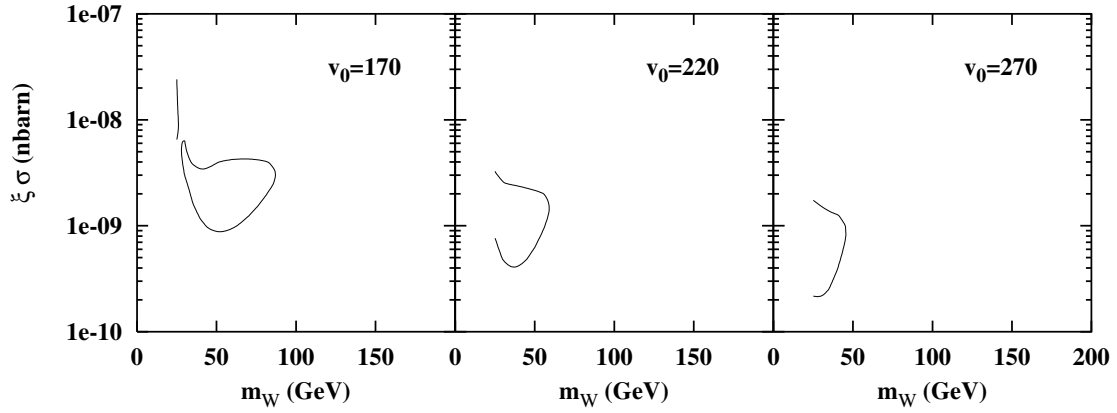


FIG. 21: The same as in Fig. 19 including a counter-rotation effect of the halo with  $\eta = 0.36$ .

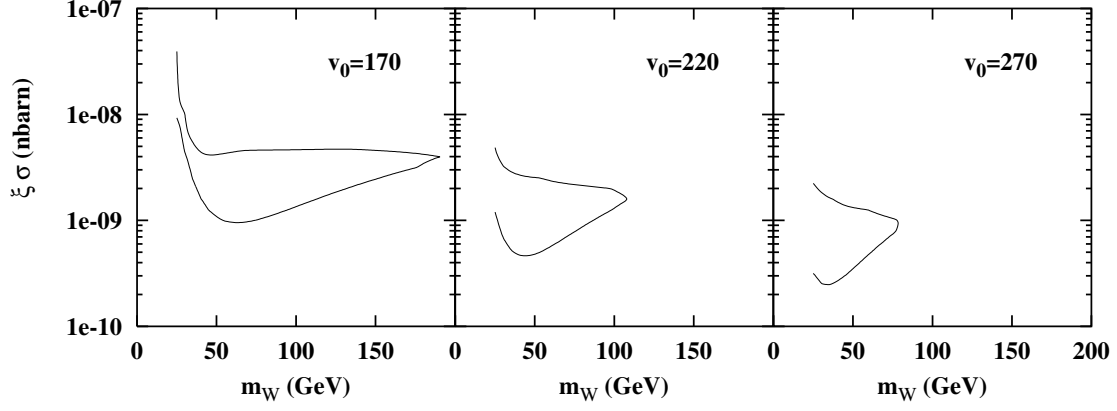


FIG. 22: The same as in Fig. 4 for the velocity distribution of model C2. Only the case  $\rho_0 = \rho_0^{max}$  is shown.

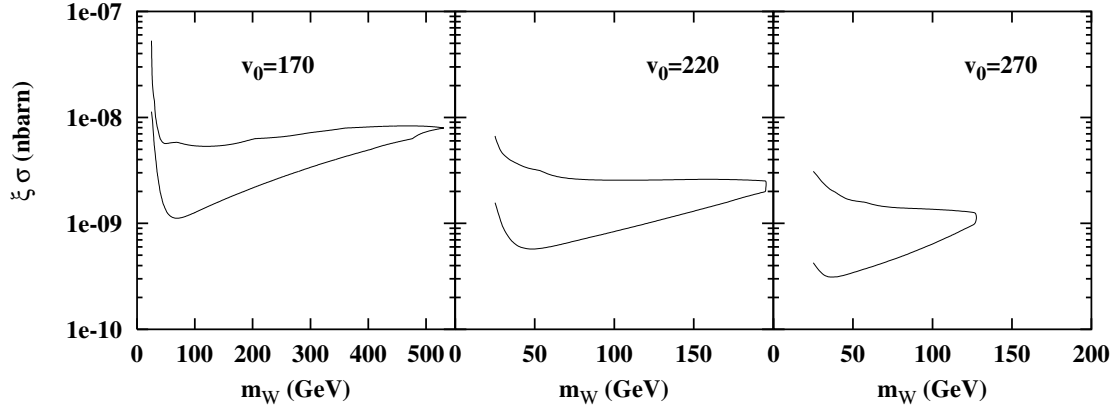


FIG. 23: The same as in Fig. 22 including a co-rotation effect of the halo with  $\eta = 0.64$ . The horizontal axis has been extended in the first panel.

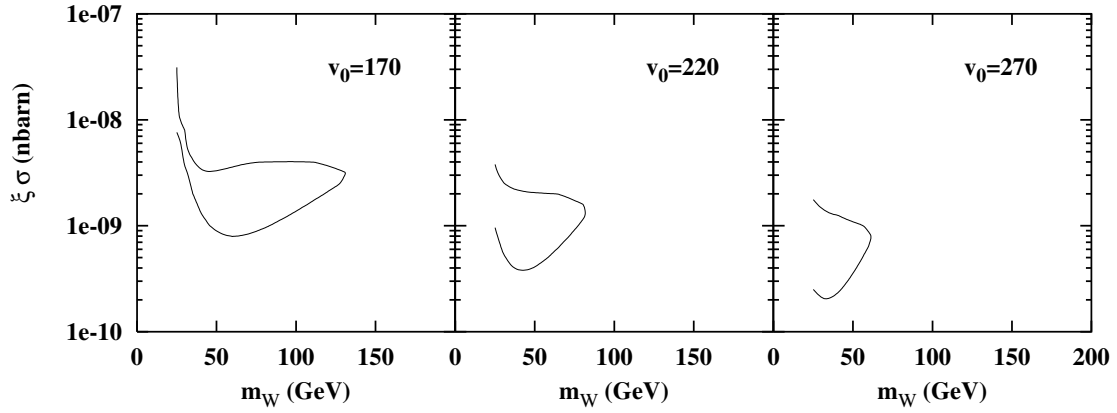


FIG. 24: The same as in Fig. 22 including a counter-rotation effect of the halo with  $\eta = 0.36$ .

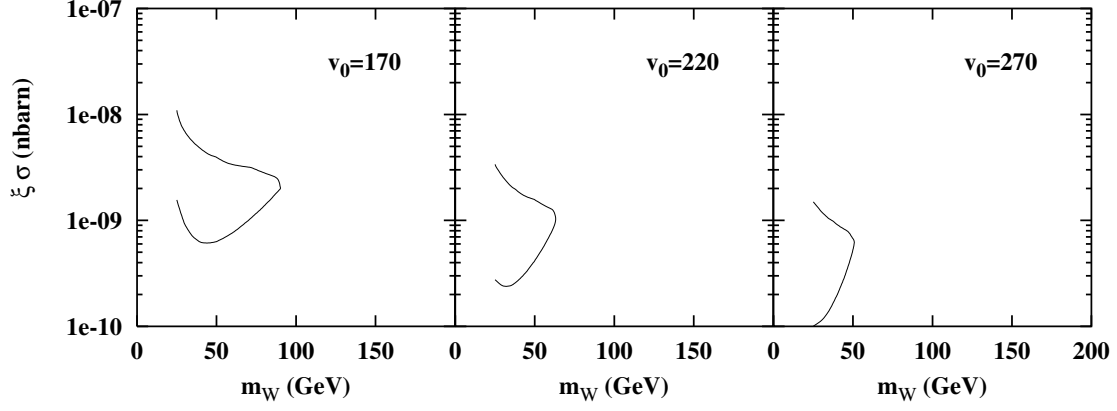


FIG. 25: The same as in Fig. 4 for the velocity distribution of model C3. Only the case  $\rho_0 = \rho_0^{max}$  is shown.

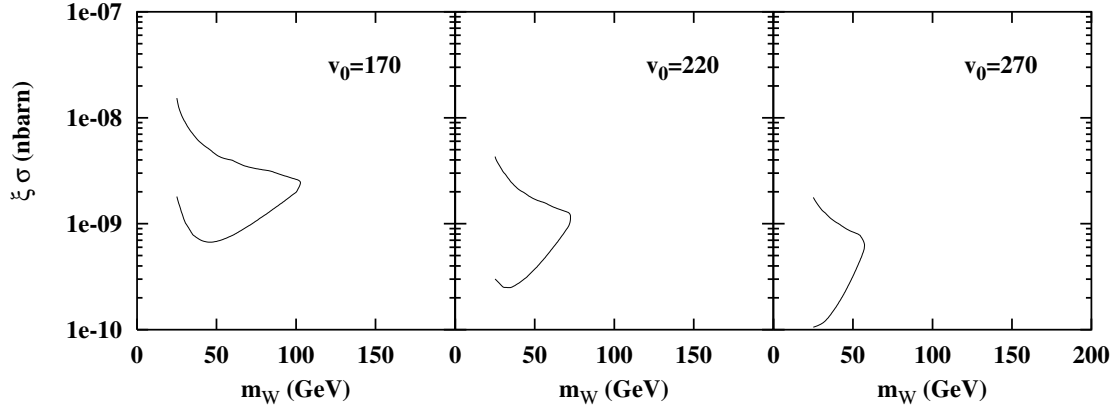


FIG. 26: The same as in Fig. 25 including a co-rotation effect of the halo with  $\eta = 0.64$ .

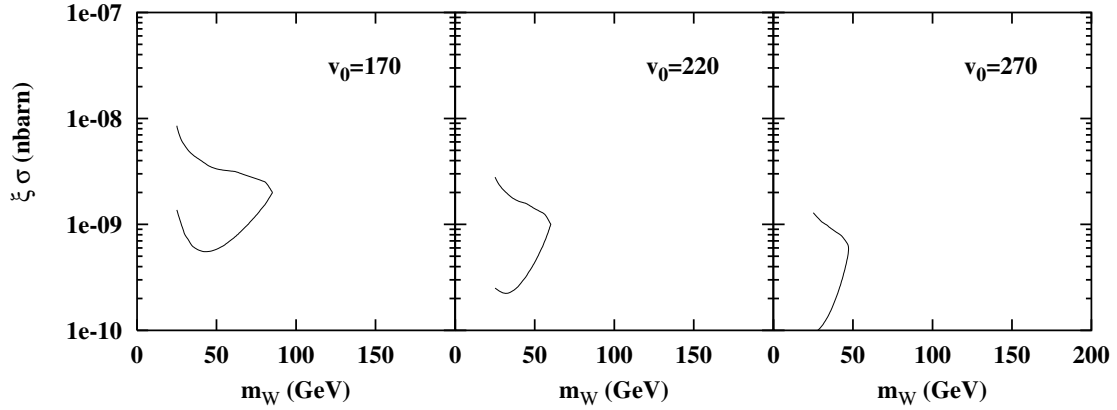


FIG. 27: The same as in Fig. 25 including a counter-rotation effect of the halo with  $\eta = 0.36$ .

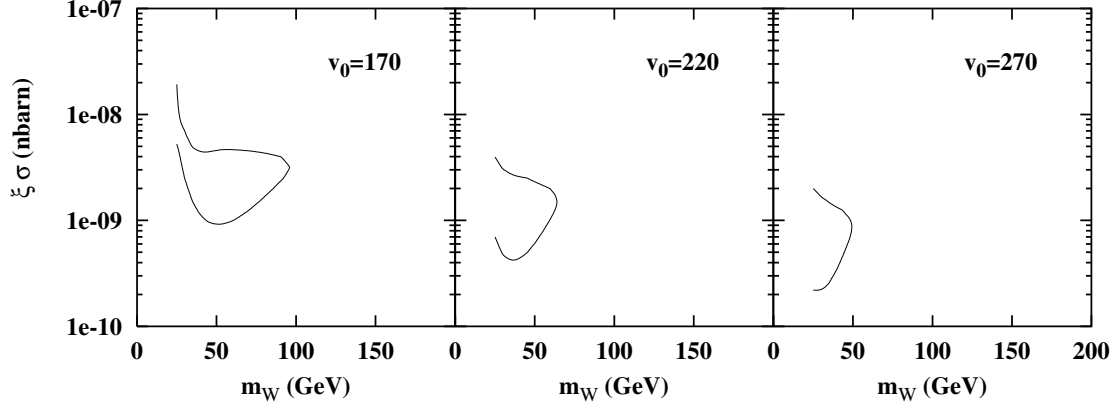


FIG. 28: The same as in Fig. 4 for the velocity distribution of model C4. Only the case  $\rho_0=\rho_0^{max}$  is shown.

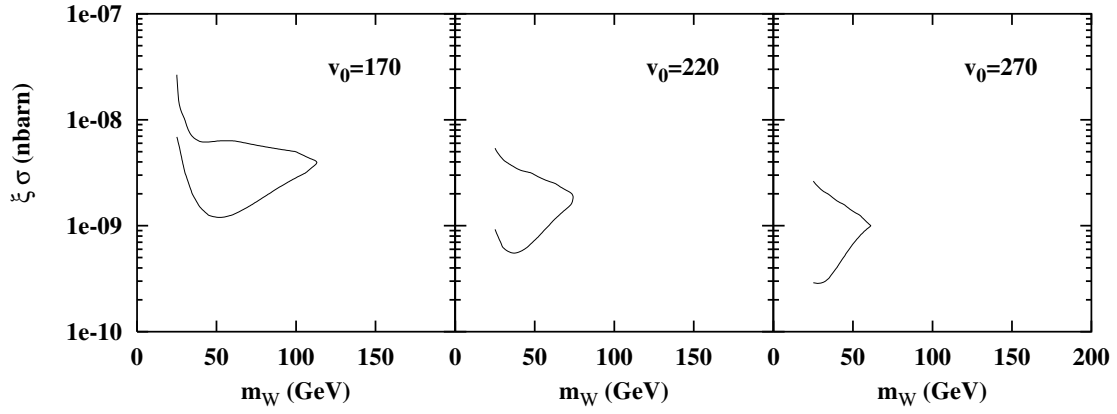


FIG. 29: The same as in Fig. 28 including a co-rotation effect of the halo with  $\eta = 0.64$ .

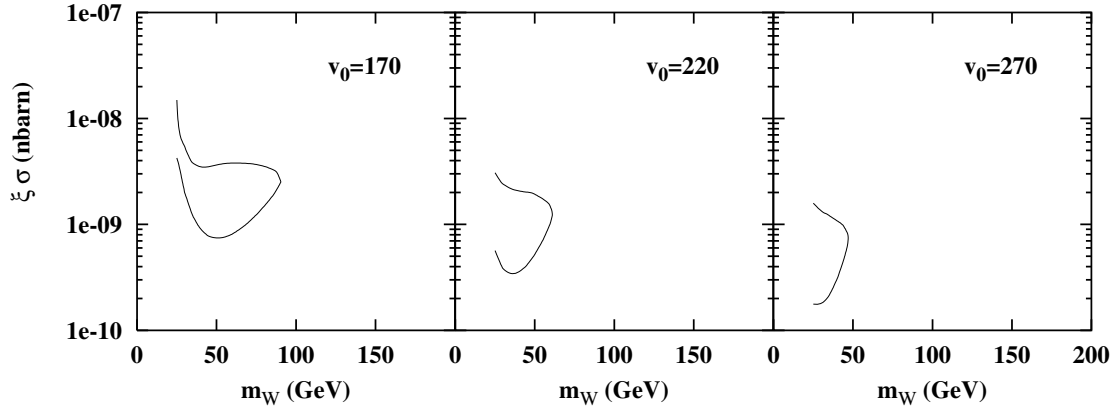


FIG. 30: The same as in Fig. 28 including a counter-rotation effect of the halo with  $\eta = 0.36$ .

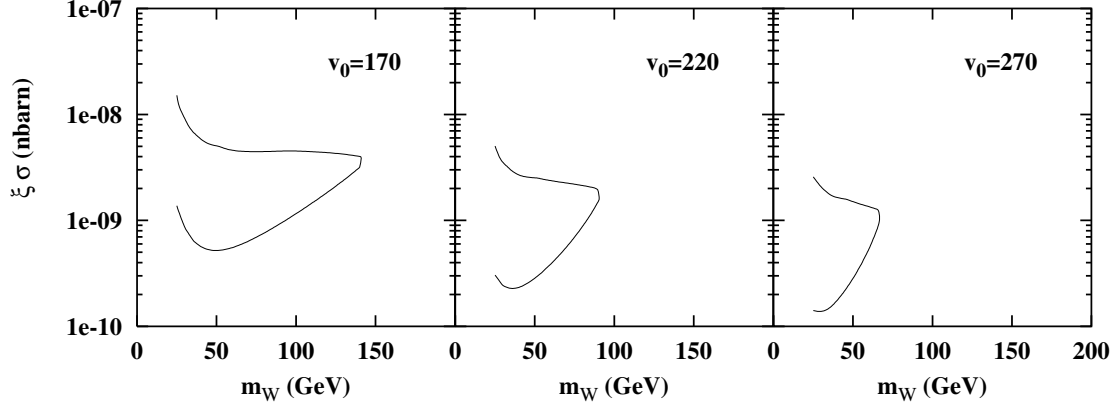


FIG. 31: The same as in Fig. 4 for the velocity distribution of model D1. Only the case  $\rho_0 = \rho_0^{max}$  is shown.

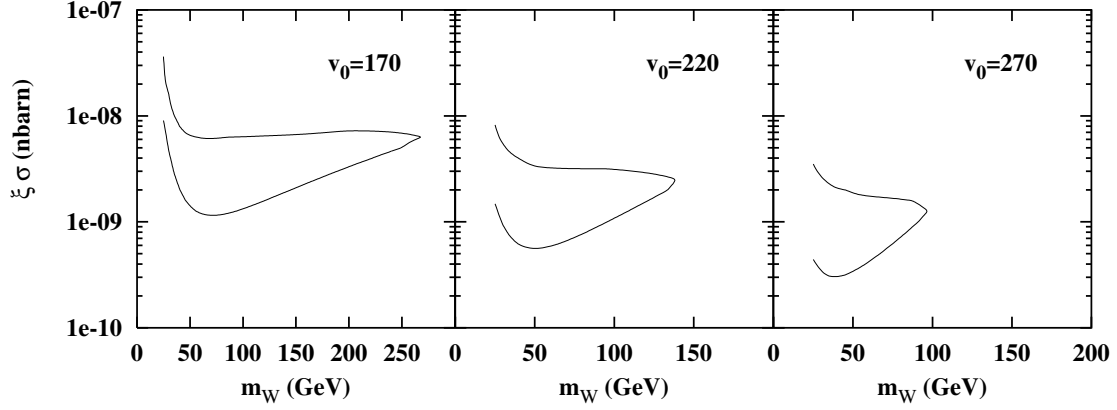


FIG. 32: The same as in Fig. 4 for the velocity distribution of model D2. Only the case  $\rho_0 = \rho_0^{max}$  is shown. The horizontal axis has been extended in the first panel.

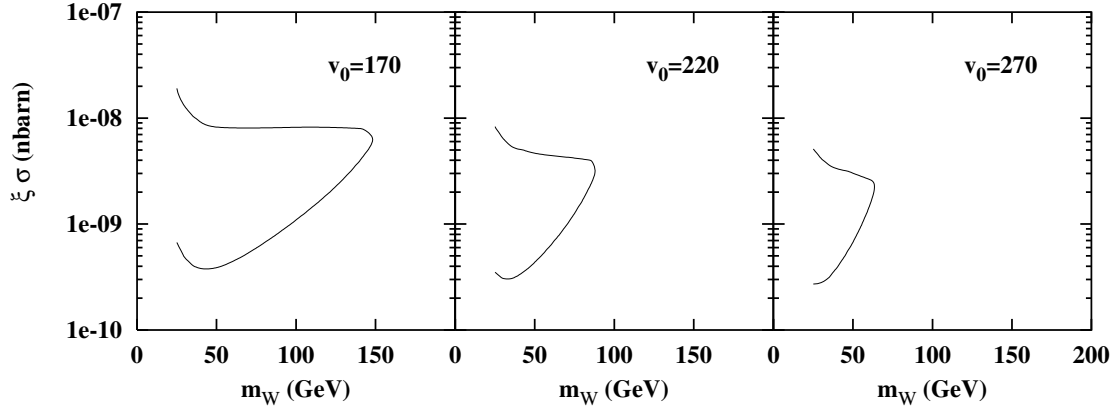


FIG. 33: The same as in Fig. 4 for the velocity distribution of model D3. Only the case  $\rho_0 = \rho_0^{max}$  is shown.

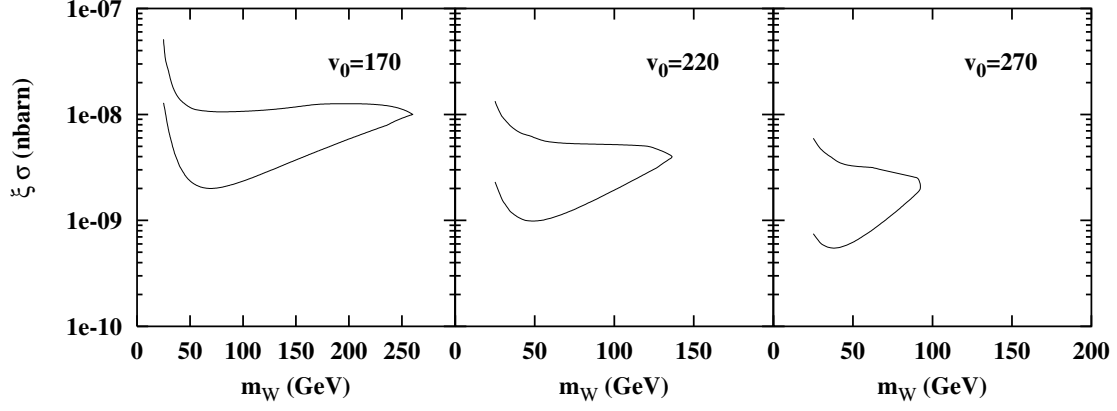


FIG. 34: The same as in Fig. 4 for the velocity distribution of model D4. Only the case  $\rho_0=\rho_0^{max}$  is shown. The horizontal axis has been extended in the first panel.

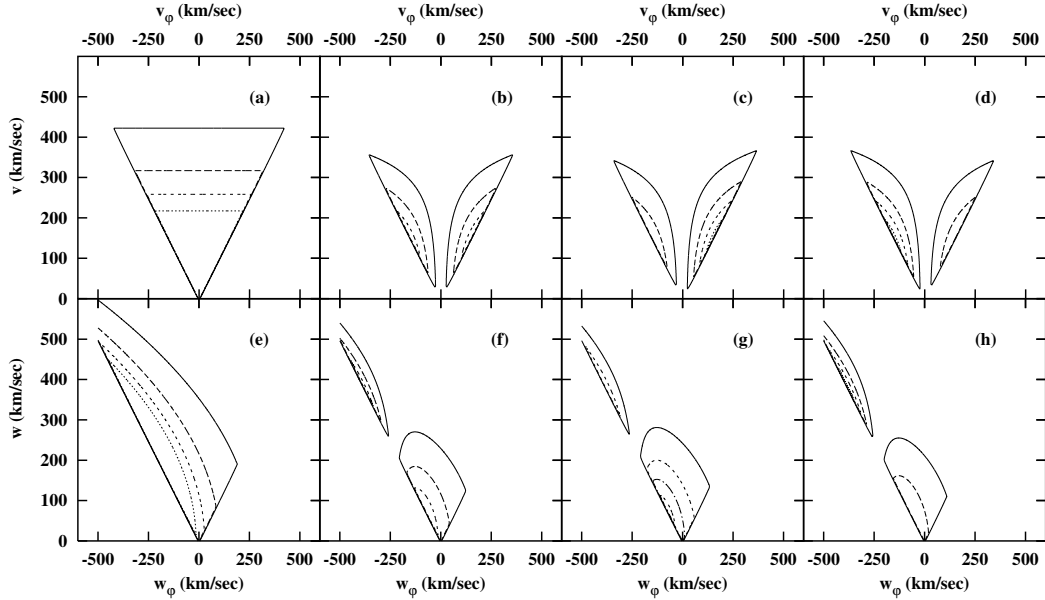


FIG. 35: Contour plots of the DF's for models B1 and C1 (see Table II). From left to right, the different panels refer to models B1 (panels (a) and (e)), C1 (panels (b) and (f)), co-rotating C1 (panels (c) and (g)), counter-rotating C1 (panels (d) and (h)). Upper panels are plotted in the  $v_\phi$ - $v$  plane, defined in the reference frame of the Galaxy, while lower panels are shown in the  $w_\phi$ - $w$  plane, defined in the reference frame of the Earth. Solid lines, big dashes, small dashes and dots correspond to growing values of the DF (in arbitrary units). The two disconnected closed contours which arise at different  $w$  values in panels (f), (g) and (h) signal the superposition in the WIMP phase space of two components with well separated r.m.s. velocities.



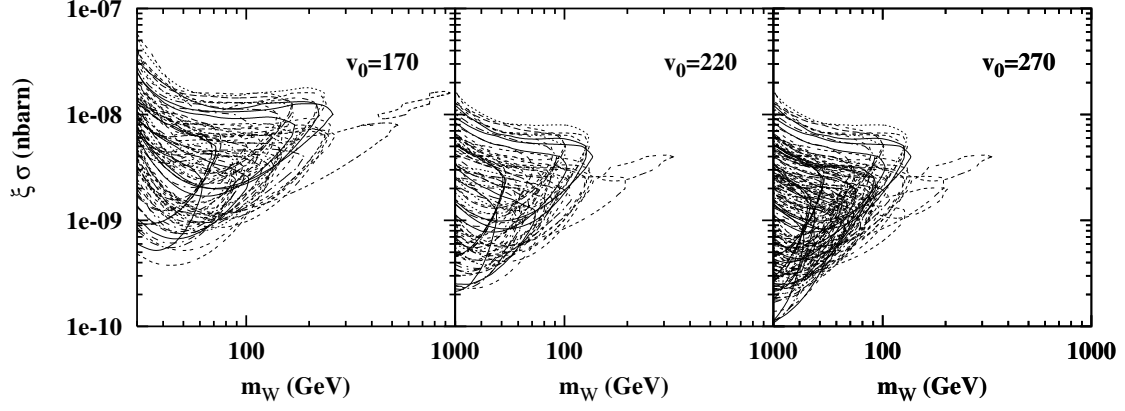


FIG. 36: Summary of the  $3\sigma$  annual-modulation regions in the plane  $\xi\sigma_{\text{scalar}}^{(\text{nucleon})}$  versus  $m_W$ , obtained by superimposing the results obtained with the velocity distributions of all the models described in Table II. For each of the models A1–7 and B1–7 two regions are plotted, which refer to the two extreme values  $\rho_0^{\text{min}}$  and  $\rho_0^{\text{max}}$  shown in Table III for the WIMP local density  $\rho_0$ . For models C1–4 and D1–4 only the regions which refer to  $\rho_0 = \rho_0^{\text{max}}$  are shown.

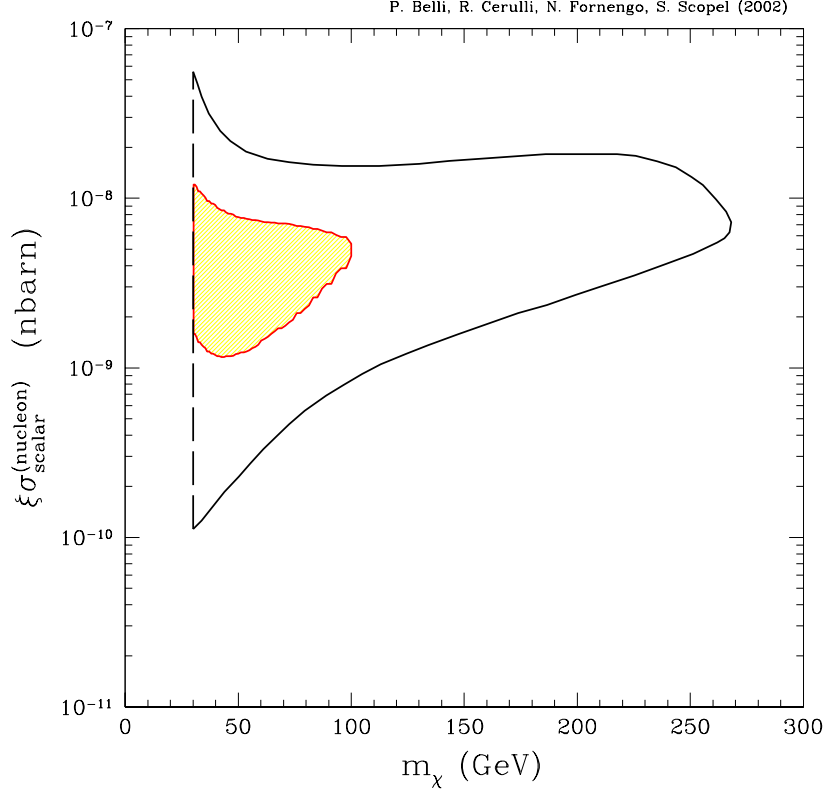


FIG. 37:  $3\sigma$  annual-modulation region in the plane  $\xi\sigma_{\text{scalar}}^{(\text{nucleon})}$  versus  $m_\chi$ , obtained by considering all the (non-rotating) galactic halo models discussed in this paper. The region is compared with the original annual modulation contour (shaded region) obtained in Ref. [1] for an isothermal sphere model of the galactic halo with rotational velocity  $v_0 = 220 \text{ km s}^{-1}$  and local dark matter density  $\rho_0 = 0.3 \text{ GeV cm}^{-3}$ .